NAVAL POSTGRADUATE SCHOOL
MONTEREY, CALIFORNIA

THESIS

DESIGN, DEVELOPMENT AND TESTING OF THE ALL-REFLECTION MICHELSON INTERFEROMETER (AMI) FOR USE IN THE MID-ULTRAVIOLET REGION
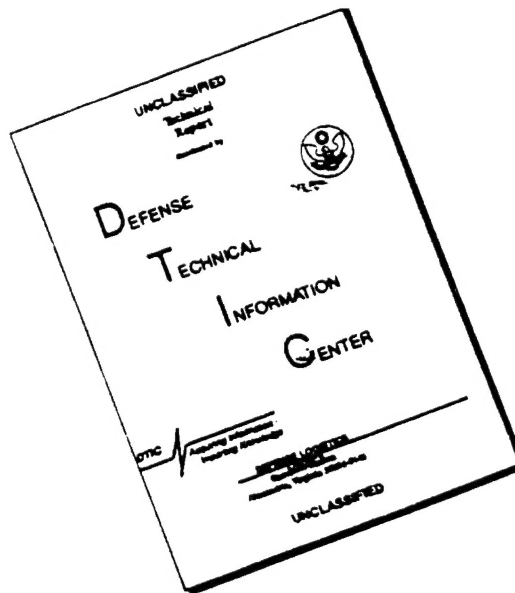
by

Jeffrey D. Hicks

December, 1995

Thesis Advisors: D. Cleary
O. Biblarz

Approved for public release; distribution is unlimited.

19960401 020

DISCLAIMER NOTICE

THIS DOCUMENT IS BEST
QUALITY AVAILABLE. THE COPY
FURNISHED TO DTIC CONTAINED
A SIGNIFICANT NUMBER OF
PAGES WHICH DO NOT
REPRODUCE LEGIBLY.

REPORT DOCUMENTATION PAGE		Form Approved OMB No. 0704-0188

Public reporting burden for this collection of information is estimated to average 1 hour per response, including the time for reviewing instruction, searching existing data sources, gathering and maintaining the data needed, and completing and reviewing the collection of information. Send comments regarding this burden estimate or any other aspect of this collection of information, including suggestions for reducing this burden, to Washington Headquarters Services, Directorate for Information Operations and Reports, 1215 Jefferson Davis Highway, Suite 1204, Arlington, VA 22202-4302, and to the Office of Management and Budget, Paperwork Reduction Project (0704-0188) Washington DC 20503.

1. AGENCY USE ONLY *(Leave blank)*	2. REPORT DATE December, 1995	3. REPORT TYPE AND DATES COVERED Master's Thesis	
4. TITLE AND SUBTITLE DESIGN, DEVELOPMENT AND TESTING OF THE ALL-REFLECTION MICHELSON INTERFEROMETER (AMI) FOR USE IN THE MID-ULTRAVIOLET REGION (u)		5. FUNDING NUMBERS	
6. AUTHOR(S) Hicks, Jeffrey D.			
7. PERFORMING ORGANIZATION NAME(S) AND ADDRESS(ES) Naval Postgraduate School Monterey CA 93943-5002		8. PERFORMING ORGANIZATION REPORT NUMBER	
9. SPONSORING/MONITORING AGENCY NAME(S) AND ADDRESS(ES)		10. SPONSORING/MONITORING AGENCY REPORT NUMBER	

11. SUPPLEMENTARY NOTES The views expressed in this thesis are those of the author and do not reflect the official policy or position of the Department of Defense or the U.S. Government.	
12a. DISTRIBUTION/AVAILABILITY STATEMENT Approved for public release; distribution is unlimited.	12b. DISTRIBUTION CODE

13. ABSTRACT *(maximum 200 words)*

The design of an All-Reflection Michelson Interferometer for use in the ultraviolet region is presented. Two different Mercury light sources, a pen-ray lamp and a germicidal lamp, were used to evaluate the performance of the instrument at 2537Å. The interferometer uses a pinhole aperture at the focus of an off-axis parabolic mirror to obtain a collimated input beam. A plane diffraction grating with sinusoidal grooves divides the beam into two orders. Planar mirrors reflect the beams back to the grating where they are directed to the detector. The beams recombine to form a linear interference pattern which is recorded by an ultraviolet detector. Data-reduction software was developed for this instrument. This software performs coherent addition of the interference pattern and creates a doubled-sided interferogram. The resulting spectrum is obtained using Fourier Transform techniques. The results of the data-reduction software suggest there is a sampling error associated with the detector. Overall, the All-Reflection Michelson Interferometer is well suited for remote sensing of mid- to extreme-ultraviolet ionospheric emissions from a sounding rocket, space shuttle or satellite platform.

14. SUBJECT TERMS Ultraviolet Spectroscopy, Interferometry, Interferometer, Fourier Transform Spectroscopy,			15. NUMBER OF PAGES 94
			16. PRICE CODE
17. SECURITY CLASSIFICATION OF REPORT Unclassified	18. SECURITY CLASSIFICATION OF THIS PAGE Unclassified	19. SECURITY CLASSIFICATION OF ABSTRACT Unclassified	20. LIMITATION OF ABSTRACT UL

NSN 7540-01-280-5500

Standard Form 298 (Rev. 2-89)
Prescribed by ANSI Std. 239-18 298-102

i

DESIGN, DEVELOPMENT AND TESTING OF THE ALL-REFLECTION MICHELSON INTERFEROMETER (AMI) FOR USE IN THE MID-ULTRAVIOLET REGION

Jeffrey D. Hicks
Lieutenant, United States Navy
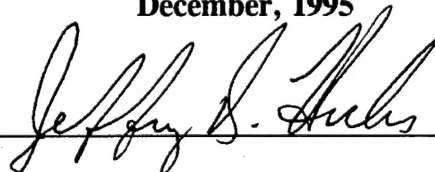B.S., Auburn University Auburn, Alabama, 1985

Submitted in partial fulfillment
of the requirements for the degrees of

MASTER OF SCIENCE IN ASTRONAUTICAL ENGINEERING
and
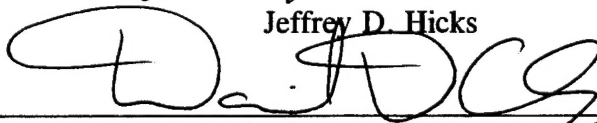## MASTER OF SCIENCE IN APPLIED PHYSICS

from the

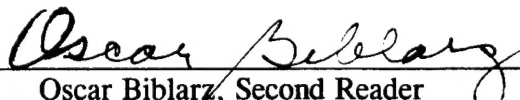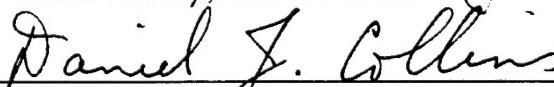## NAVAL POSTGRADUATE SCHOOL
December, 1995

Author: _____

Jeffrey D. Hicks

Approved by: _____

David D. Cleary, Thesis Advisor

_____

Oscar Biblarz, Second Reader

_____

Daniel J. Collins, Chairman
Department of Aeronautics and Astronautic

_____

William B. Colson, Chairman
Physics Department

iii

ABSTRACT

The design of an All-Reflection Michelson Interferometer for use in the ultraviolet region is presented. Two different Mercury light sources, a pen-ray lamp and a germicidal lamp, were used to evaluate the performance of the instrument at 2537 Å. The interferometer uses a pinhole aperture at the focus of an off-axis parabolic mirror to obtain a collimated input beam. A plane diffraction grating with sinusoidal grooves divides the beam into two orders. Planar mirrors reflect the beams back to the grating where they are directed to the detector. The beams recombine to form a linear interference pattern which is recorded by an ultraviolet detector. Data-reduction software was developed for this instrument. This software performs coherent addition of the interference pattern and creates a doubled-sided interferogram. The resulting spectrum is obtained using Fourier Transform techniques. The output of the data-reduction software suggest there is a sampling error associated with the detector. Overall, the All-Reflection Michelson Interferometer appears well suited for remote sensing of mid- to extreme-ultraviolet ionospheric emissions from a sounding rocket, space shuttle or satellite platform.

TABLE OF CONTENTS

vii

LIST OF FIGURES

TABLE OF ABBREVIATIONS

AMI	All-Reflection Michelson Interferometer
ARGOS	Advanced Research and Global Observation Satellite
CCD	Charge Coupled Device
CsTe	Cesium Telluride
DART	Dudley Atckinson Ray Trace
EUV	Extreme Ultraviolet
FFT	Fast-Fourier Transform
FTS	Fourier Transform Spectrometer
Hg	Mercury
HIRASS	High Resolution Airglow/Aurora Spectroscopy
IDL	Interactive Data Language
ISAAC	Ionospheric Spectroscopy and Atmospheric Composition
MCP	Microchannel Plate
MgF_2	Magnesium Flouride
MOS	Metal Oxide Semiconductor
MTF	Modulation Transfer Function
MUSTANG	Middle Ultraviolet Spectrograph
MUV	Middle Ultraviolet
NIST	National Institute of Standards and Technology
NPS	Naval Postgraduate School
OPD	Optical Path Difference
RbTe	Rubidium Telluride
SHS	Spatial Heterodyne Spectroscopy
SORL	Space Optics Research Lab
TIFF	Tagged Image File Format

ZPD   Zero Path Difference

I. INTRODUCTION

The Physics Department at the Naval Postgraduate School (NPS) has been actively involved in research associated with the ionosphere for many years. Beginning in 1990, the first of three sounding rocket experiments was conducted. These experiments involved the use of the Middle Ultraviolet Spectrograph (MUSTANG) instrument shown in Figure 1.
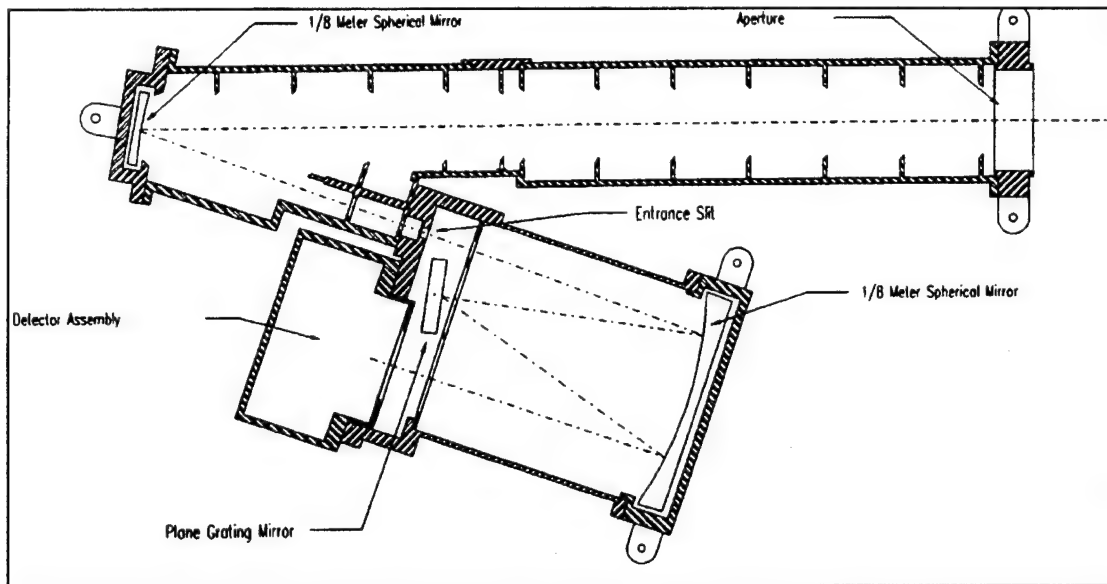
Figure 1: MUSTANG Instrument. Taken From Atckinson (1993).

The spectral resolution of this instrument was approximately 10 Å and provided measurements of the emissions from 1800 to 3400 Å [Cleary et. al., 1995]. A typical spectrum of this instrument is shown in Figure 2. The successor to this instrument is the Ionospheric Spectroscopy and Atmospheric Composition (ISAAC) instrument. ISAAC is a part of a Naval Research Laboratory/NPS experiment known as High Resolution Airglow/Aurora Spectroscopy (HIRAAS). The HIRAAS experiment payload, shown in Figure 3, is scheduled for a 1996 launch onboard an Air Force's Advanced Research and Global Observation Satellite (ARGOS). The ISAAC instrument has a resolution of

approximately 2.5 Å [MacQuarrie, 1994]. Both the MUSTANG and ISAAC instruments made use of conventional grating spectrometer technology to measure the ionospheric emissions over a large wavelength range.
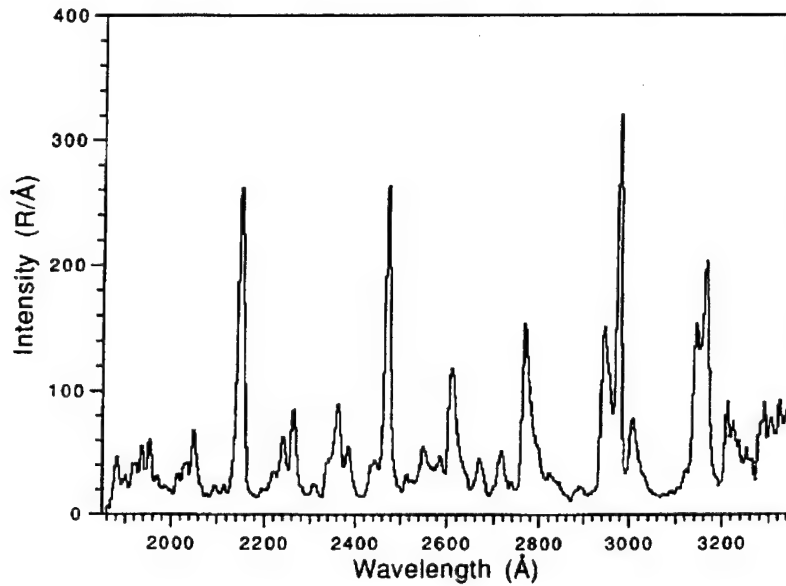
Figure 2: Typical Spectrum From MUSTANG Instrument. Taken From Hymas (1994).
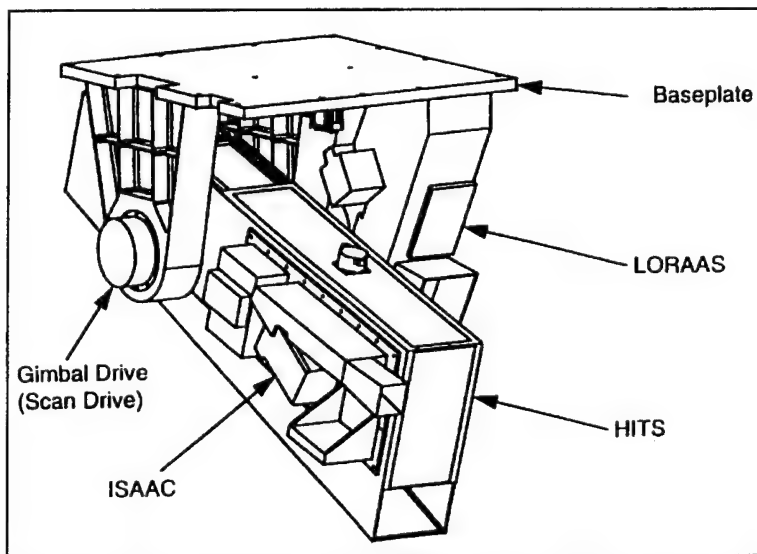
Figure 3: ISAAC Instrument as a Part of the HIRAAS Payload Onboard the ARGOS Satellite. Private Communication With NRL (1993).

2

In order to investigate the detailed shape of the line profile of an ultraviolet emission, an instrument with considerably higher resolution was needed. Nichols (1990) was the first to investigate high resolution instrument designs at NPS. His efforts resulted in the development of a Rowland Circle Interferometer. Due to difficulties with the resulting interference pattern, Wallace (1992) abandoned the design in favor of a new design, the All-Reflection Michelson Interferometer (AMI). The AMI underwent several engineering upgrades with Risley (1993) and Gill (1994). The culmination of their efforts was a prototype instrument that operated with incoherent visible light sources.

A. THESIS OBJECTIVES

The objective of this thesis was to continue the development of the AMI and to extend its operational capability into the mid-ultraviolet wavelength range. All of the design changes had to meet the requirements of high resolution, high sensitivity of low intensity emissions and suitable for operations in space environments. This last requirement forced the design to be compact, lightweight and economical. In addition, upgrading of data-reduction software was necessary to perform coherent addition of the interference pattern.

B. THESIS OUTLINE

This thesis is divided into eight chapters and one appendix. The first chapter is the introduction. Chapter two provides the background information for the design and development of the AMI. These areas include two beam interference, diffraction grating theory and ultraviolet sensitive detector technology. A history of the all-reflection interferometer is provided in chapter three. Chapter four discusses the work performed on the AMI as part of this thesis. This research is broken down into two iterations. The first was concerned with obtaining an interference pattern using an ultraviolet source

3

while the second strove to perfect the instrument. Chapter five describes the development of the data-reduction software used to obtain the spectrum from the interference pattern created by the AMI. To perform this data reduction, a one-dimensional interferogram is generated and used as input to the Fast Fourier Transform Algorithm. Chapter six contains the spectral results obtained from two different Mercury sources at 2537 Å. Chapter seven documents the suggestions for a future third design and development iteration. The goal of this iteration will be to increase the AMI's resolution, replace the light source and correct or mitigate the sampling error. Finally, the eighth chapter lists a summary of the experimental results and recommends topics for future studies. One appendix is included which contains a listing of the data-reduction programs SPECTRA2.PRO, IMAGE.PRO and DELTA3.PRO.

4

II. BACKGROUND

This chapter describes physical principles behind the operation of the All-Reflection Michelson Interferometer. A general overview of the mathematics describing the formation of an interference pattern from two planar light waves is provided. Additionally, a discussion of grating theory is included since this the corner stone for the operation of the AMI. Finally, a detailed description of the ultraviolet sensitive detector is included.

A. TWO-BEAM INTERFERENCE

Formation of an interference pattern involves the superposition of the electric fields of two or more separate light beams. For this thesis, only two beam interference is considered. The beams are split from the source by a diffraction grating. These beams follow different optical paths before recombining. As a result, the two beams have different optical path lengths. This difference in optical path length results in a difference in the phases of the two fields at the recombination point. The detector senses the time-averaged power density of the resultant electric field to produce an intensified image of the interference pattern. The following is a mathematical discussion of the formation of the two-beam interference pattern after Klein (1986).

Consider two electromagnetic waves represented by the vectors $\mathbf{E}_1$ and $\mathbf{E}_2$. The bold face type designates vector quantities. A plane wave is represented as

$$\mathbf{E} = \mathbf{A} \cos (\omega t - \mathbf{k} \cdot \mathbf{r} + \theta).$$

For clarity, the vector nature of the field is suppressed in the remainder of this discussion. Alternatively, the electric field can be expressed using complex notation as $E = A\, e^{i\phi}$ where

$$\phi = \omega t - \mathbf{k} \cdot \mathbf{r} + \theta.$$

The fields of two beams,

5

$$E_1 = A_1 \, e^{i\phi_1} \quad \text{and} \quad E_2 = A_2 \, e^{i\phi_2},$$

can be represented in the complex plane as shown in Figure 4.a.
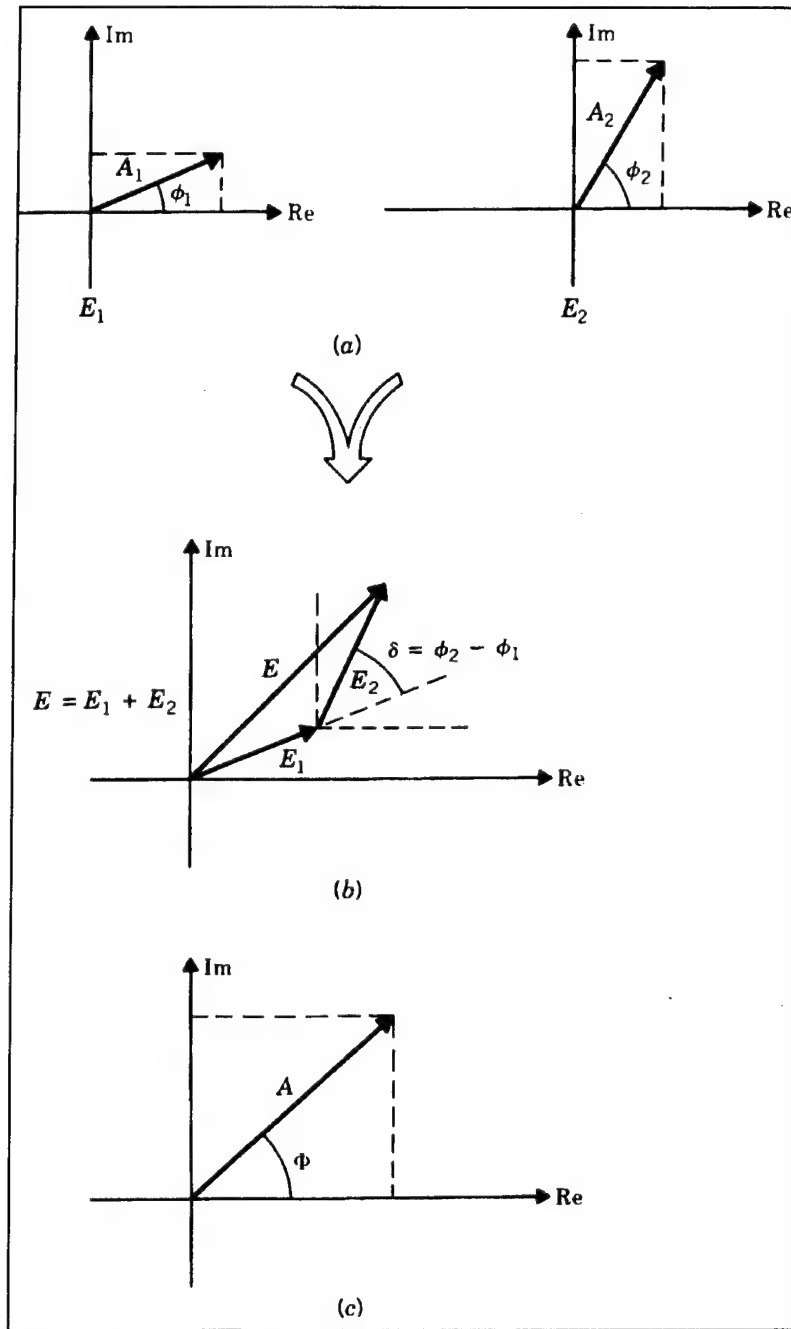
Figure 4: Electric Field Superposition Using Phasors. Taken From Klein (1986).

A graphical representation of the principle of superposition is shown in Figure 4.b, where the electric field at the recombination point is

$$E = E_1 + E_2.$$

The magnitude and phase of the resultant electric field, shown in Figure 4.c, can be represented as

$$E = A\, e^{i\phi} = A\,(\cos\phi + i \sin\phi). \qquad (1)$$

By inspection, the magnitude is given by

$$A = [\,(Re\ E)^2 + (Im\ E)^2\,]^{1/2} \qquad (2)$$

and the phase is

$$\phi = \tan^{-1}(Im\ E\,/\,Re\ E) = \cos^{-1}(Re\ E/A). \qquad (3)$$

The real and imaginary parts of E can be broken down into components of the original electric fields. The real and imaginary parts of E become

$$Re\ E = A_1 \cos\phi_1 + A_2 \cos\phi_2 \qquad (4)$$

$$Im\ E = A_1 \sin\phi_1 + A_2 \sin\phi_2. \qquad (5)$$

Substitution of Equations (4) and (5) into Equation (2), leads to

$$A^2 = A_1^{\,2} + A_2^{\,2} + 2\,A_1 A_2 \cos\delta. \qquad (6)$$

Here δ is the angle representing the phase difference between the two electric fields as shown in Figure 4.b. After some manipulation of Equation (3), the phase can be expressed by

$$\phi = \omega t + \phi' \qquad (7)$$

where

$$\phi' = \sin\delta\,/\,(A_1/A_2 + \cos\delta).$$

In order to simplify the evaluation of the time-averaged power density, the complex phasor notation is replaced with the traditional sinusoidal notation. Only the real component of the electric field is now considered. After substituting Equation (7) into Equation (1), the electric field becomes

$$E = A \cos(\omega t + \phi').$$

7

Applying the trigonometric identity for the cosine of the sum of two angles, this electric field can be rewritten as

$$E = A \left[\cos \omega t \cos \phi' - \sin \omega t \sin \phi'\right]. \qquad (8)$$

The time-averaged power density is given by

$$<S> = c \epsilon <E^2>. \qquad (9)$$

To evaluate $<S>$, the time-average of the electric field squared must first be determined. Squaring Equation (8) gives

$$E^2 = A^2 \left[\cos^2 \omega t \cos^2 \phi' + \sin^2 \omega t \sin^2 \phi'\right.$$
$$\left. - 2 \cos \omega t \sin \omega t \cos \phi' \sin \phi'\right]. \qquad (10)$$

The time-average of Equation (10) can now be easily evaluated. Using the following trigonometric identities:

$$<\sin^2 \omega t> = <\cos^2 \omega t> = 1/2$$

$$<\cos \omega t \sin \omega t> = 0$$

and

$$\cos^2 \phi' + \sin^2 \phi' = 1.$$

we find

$$<E^2> = A^2 / 2. \qquad (11)$$

Substituting Equation (11) into Equation (9), the time-averaged power density is simplified to

$$<S> = c \epsilon A^2 / 2$$

or substituting Equation (6)

$$<S> = c \epsilon [A_1^2 + A_2^2 + 2 A_1 A_2 \cos \delta] / 2.$$

For the special case where $A_1 = A_2$, the time-averaged power density is expressed by

$$<S> = 2 <S_1> [1 + \cos \delta]$$

or

$$<S> = 4 <S_1> \cos^2 (\delta/2) \qquad (12)$$

8

A plot of Equation (12) is shown in Figure 5.
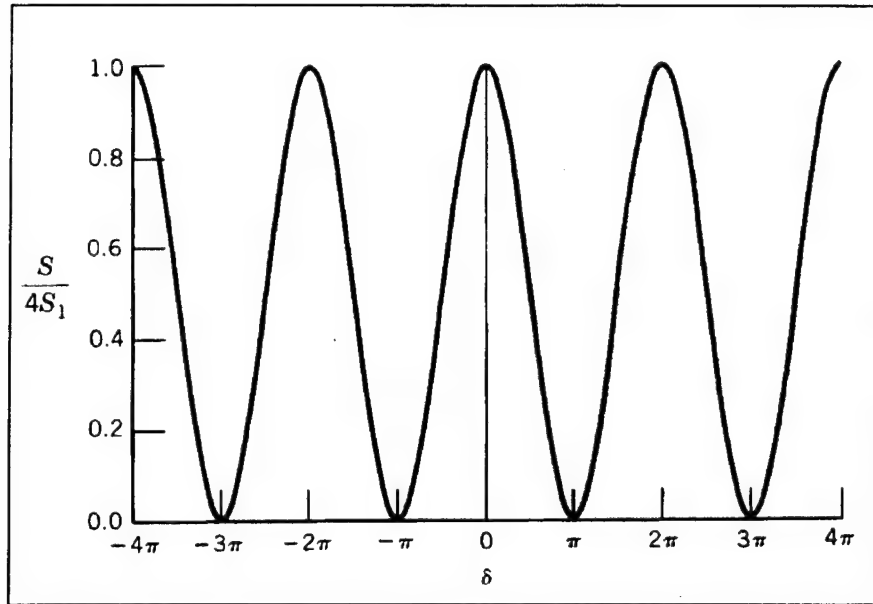
Figure 5: Power Density Distribution for Two-Beam Interference. Taken From Klein (1986).

Note, the time-averaged power density has maxima and minima where δ is an even and odd integer multiple of π, respectively. These maxima and minima correspond to the familiar light and dark fringes of an interference pattern.

B. GRATING THEORY

The sinusoidal diffraction grating is the corner stone component of the AMI. A fundamental aspect of our design is the ability of the diffraction grating to separate light into beams of monochromatic light called orders. While, the first diffraction grating was constructed by the astronomer David Rittenhouse in 1785, the idea of its use as a beam splitter for spectroscopy was not proposed until 1911 [Barus, 1911]. The following is a description of the physical principles of a diffraction grating based on the <u>Diffraction Grating Handbook</u>, from the Milton Roy Company (1994).

Consider the plane grating shown in Figure 6. For simplicity this V-groove grating will be discussed, but the same conclusions hold for a sinusoidal grating.

9
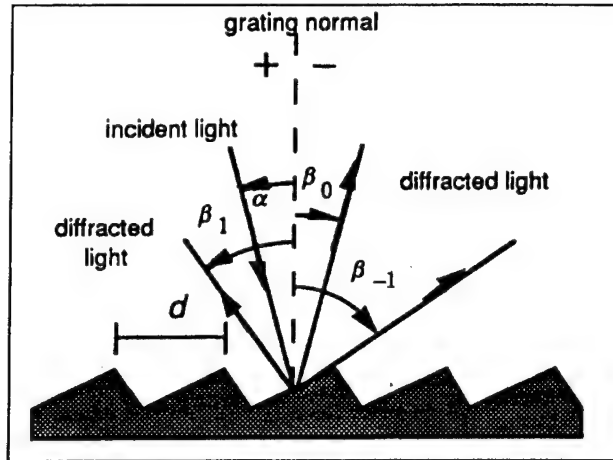
Figure 6: Geometry of Planar Diffraction Grating. Taken From Milton Roy Company (1994).

Each grating groove can be pictured as a small, slit-shaped source of diffracted light. These grooves are separated by the distance d. A light source, of wavelength λ, with an incidence angle, α, will be diffracted by the grating into the angles β_m where m is the diffraction order number. The sign for each angle, β_m, depends on whether the diffracted light is on the same or opposite side of the grating normal as the incident light. β_m is positive if the diffracted light is on the same side of the grating normal as the incident light and is negative if on the opposite side. Similarly, the sign for m depends on whether the diffracted light is on the same or opposite side of the m=0 beam as the incident light.
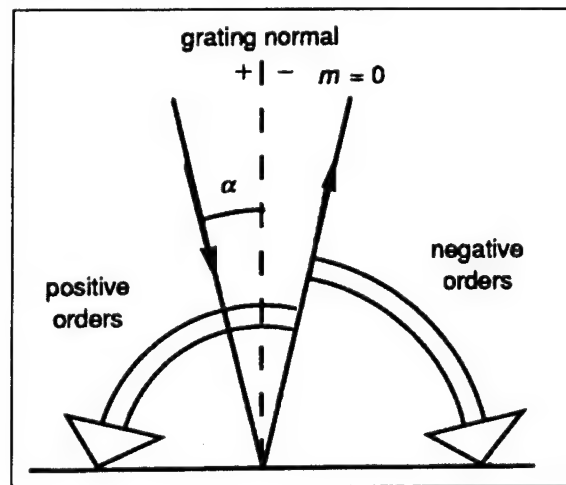
Figure 7: Sign Convention for Spectral Order m. Taken From Milton Roy Company (1994).

10

If the m_{th} order beam is on the same side then m is positive otherwise m is negative. Figure 7 shows a graphical representation of the convention used for the sign of m.

A closer look at the diffraction grating wavefront geometry is shown in Figure 8.
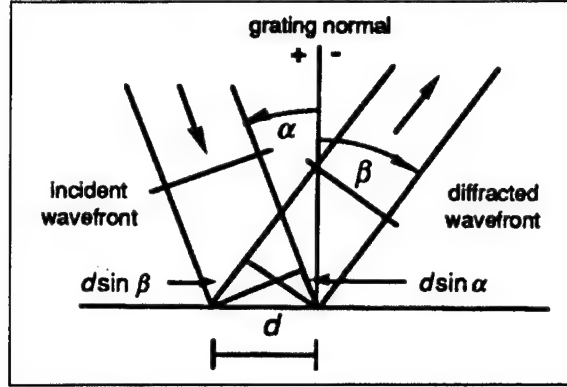
Figure 8: Geometry of Diffraction. Taken From Milton Roy Company (1994).

The path length difference between two beams from adjacent grooves is

$$d (\sin \alpha + \sin \beta).$$

Only when this path length difference is equal to an integral multiple of the wavelength of incident light will these beams be in phase. At all other angles, there is some measure of destructive interference. Therefore, the diffracted beams will only exist at the angles β_m as prescribed by the grating equation

$$m \lambda = d (\sin \alpha + \sin \beta_m). \tag{13}$$

By defining G, the groove frequency in grooves / mm, as $1 / d$, Equation (13) becomes

$$G m \lambda = \sin \alpha + \sin \beta_m. \tag{14}$$

The maximum value possible for $\sin \alpha + \sin \beta_m$ is 2. It follows that,

$$| G m \lambda | < 2. \tag{15}$$

Hence for a given G and λ, only certain values of m are allowed. This means for a given grating and operating wavelength a certain number of diffraction beams will exist. Alternatively, if only a certain number of diffraction beams are desired for a fixed operating wavelength, Equation 15 can be used to find the G that satisfies this condition.

11

Equation (14) allows for the possibility of multiple diffraction orders. Notice from Figure 9 that for every first order beam at a wavelength λ, there is a second order beam at a wavelength $\lambda/2$ that has the same diffraction angle β. This is known as overlapping spectral orders. For the application in the AMI, the possibility of overlapping spectral orders must be carefully considered.
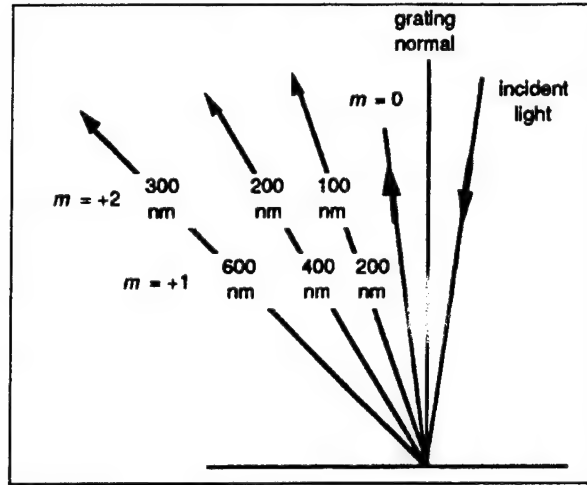
Figure 9: Overlapping of Spectral Orders. Taken From Milton Roy Company (1994).

An optical designer must also consider the effects of stray light on the operation of the instrument. If the instrument is not designed properly, stray light can reflect off the instrument's optical surfaces and eventually end up in the image plane. Another consequence of Equation (14) is the possibility of undesired diffraction orders. These undesired orders are also potential sources of unwanted stray light. These problems may be alleviated by choosing the proper groove frequency to eliminate unwanted orders and also trapping unwanted orders through baffling and proper instrument design.

C. ULTRAVIOLET DETECTOR

This section discusses the detector used to observe the ultraviolet interference pattern produced by the AMI. For this thesis, the AMI was configured to analyze the Mercury emission at 2537 Å. This is well below the short-wavelength limit ($\sim$ 4000 Å)

of the spectral response for a charge coupled device (CCD) detector. Hence, a new ultraviolet sensitive detector had to be designed and developed for this application. The resulting detector unit is composed of an image intensifier that is fiber-optically coupled to the face plate of a CCD camera. The detector's output, an image containing 753x244 pixels, is processed by computer software for display and storage. Each of the detector components is considered separately in detail below.

1. Detector Operation

The image intensifier is a proximity focused channel intensifier tube with dual microchannel plates. It was manufactured by the Electro-Optical Products Division of ITT. The basic intensifier consists of a quartz input window, a photocathode, two microchannel plates, a phosphor screen and a fiber-optic face plate for output. A quartz window is used to allow ultraviolet light to enter the detector since glass is opaque at mid-ultraviolet wavelengths. The incident light encounters the Cesium Telluride (CsTe) photocathode and generates an electron signal. Figure 10 shows a plot of the quantum efficiency of the CsTe photocathode as a function of wavelength. The CsTe photocathode was specifically chosen to ensure that the detector would be solar blind or insensitive to visible light.
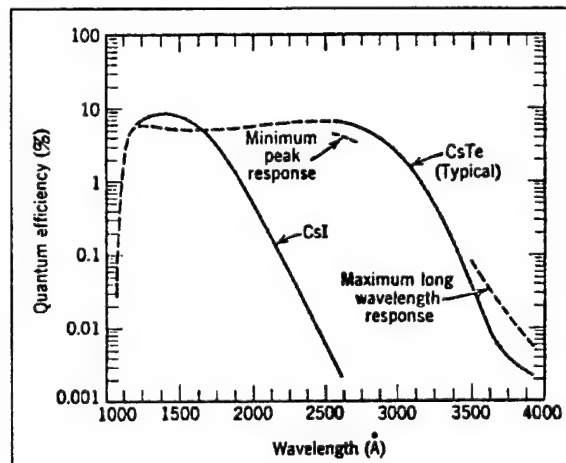
Figure 10: Quantum Efficiency Curve for Coatings of Photocathode. Taken From Samson (1967).

13

The emitted primary electrons from the photocathode are directed to the microchannel plate (MCP) assembly. A drawing of a microchannel plate is shown in Figure 11.
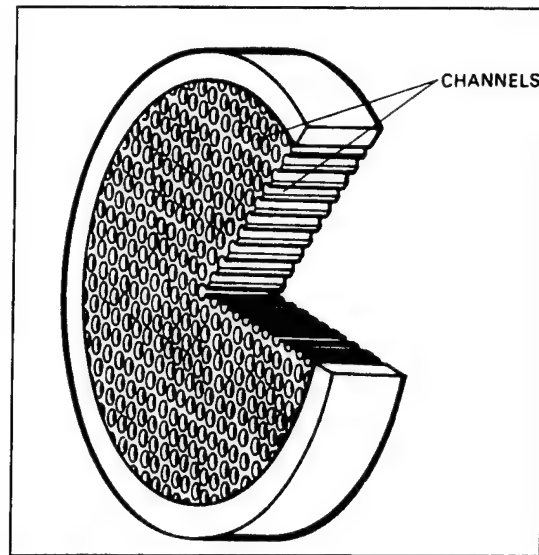
Figure 11: MCP Construction. Taken From Hamamatsu Photonics (1985).

This plate consists of millions of glass capillaries (channels) with an inner diameter of approximately ten micrometers. Each tube acts as an independent photo-multiplier. As seen in Figure 12, an electric field is established along the channel axis by applying a voltage (1100 - 1700 Vdc) across the input and output faces of the MCP assembly. This electric field accelerates the electrons.
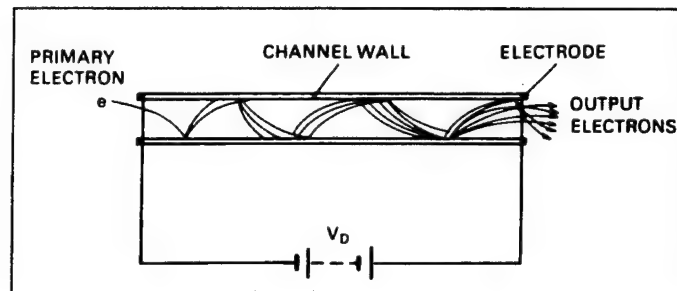
Figure 12: Electric Representation of Electron Amplification. Taken From Hamamatsu Photonics (1985).

The accelerating electrons, following a parabolic path, eventually strike the channel wall causing secondary electrons to be formed. This process is repeated many times down the tube length causing the number of electrons to increase exponentially. This amplified

14

electron beam is subsequently focused onto an aluminum screen coated with P-20 luminescent phosphor. Here the electron beam is converted into the visible image for output. The visible image is directed to the output of the intensifier via a 25 millimeter circular fiber-optic faceplate. A high quality fiber-optic taper with a demagnification ratio of 1.6 is used to transfer the image to the 11 millimeter cross-diagonal face plate of the CCD chip. The CCD chip is installed in an EDC-1000HR camera marketed by the Electrim Corporation. The TI-241 CCD chip, manufactured by Texas Instruments, consists of a two dimensional array of closely spaced metal oxide semiconductor (MOS) capacitors. Because the incoming photons have energies that are greater than the bandgap energy of the silicon material of the MOS capacitor, they are absorbed and thereby generate electron-hole pair. The electrons are collected in an energy well generated by the MOS capacitor during the integration portion of the operation cycle. The amount of charge collected in the packet is proportional to the intensity of light incident upon that individual MOS capacitor. During the scan period, each charge packet is transferred to the output to be processed by the computer as shown in Figure 13. Using an analog-to-digital converter, the output is transformed into an 8 bit signal and is used for display or stored in a tagged image file format (TIFF) file for later analysis.
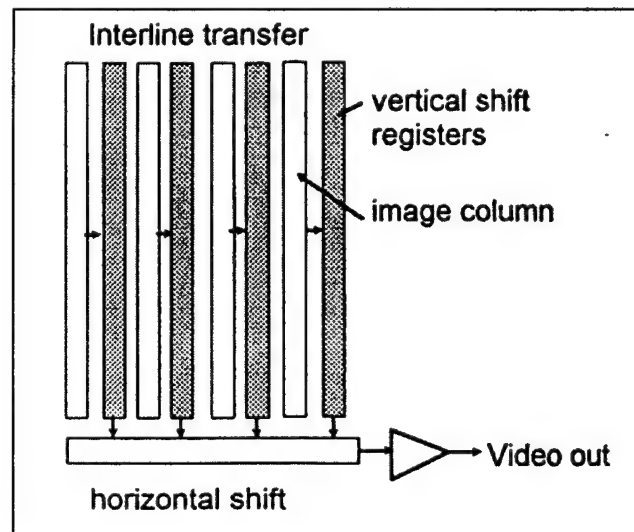
Figure 13: CCD Data Output Circuit. Taken From Walters, (1990).

2. MCP Construction

The fabrication of an MCP assembly is shown in Figure 14. It begins with the insertion of an acid soluble core rod into a silicate glass tube. The presence of this solid core reduces channel distortion during the drawing and extrusion processes of fabrication. The pair is then drawn and high temperature fused to form a mono-fiber. By stacking many of these mono-fibers together, an array is created that is in turn drawn into a multi-fiber. A so-called billet is constructed by combining many multi-fibers inside a glass retainer. The voids of the billet are filled with filler glass. The billet is fused and sliced into wafers and then ground and polished to an optical finish. The solid core is removed by placing the wafer into a weak acid solution. The acid soluble core is dissolved leaving behind the completed honeycomb shaped microchannel array. To enhance the secondary electron emission process, a thin layer of silica-rich glass is deposited on the surface of the channel wall. A high temperature hydrogen reduction process subsequently reduces the lead oxide levels in the glass. This promotes the electron conductivity in the current carrying layer that lies just beneath the electron emission layer of the channel wall. Finally, the metal electrodes are vacuum deposited onto the input and output surfaces of the MCP. This provides a terminal location on which to apply the voltages used for the amplification process.

Monofiber Draw

Multifiber Draw

Billet Fabrication

Billet Slice, Grind, Polish

Chemical Processing

Hydrogen Reduction

Electrode Evaporation

Electrical Test

Final Inspection
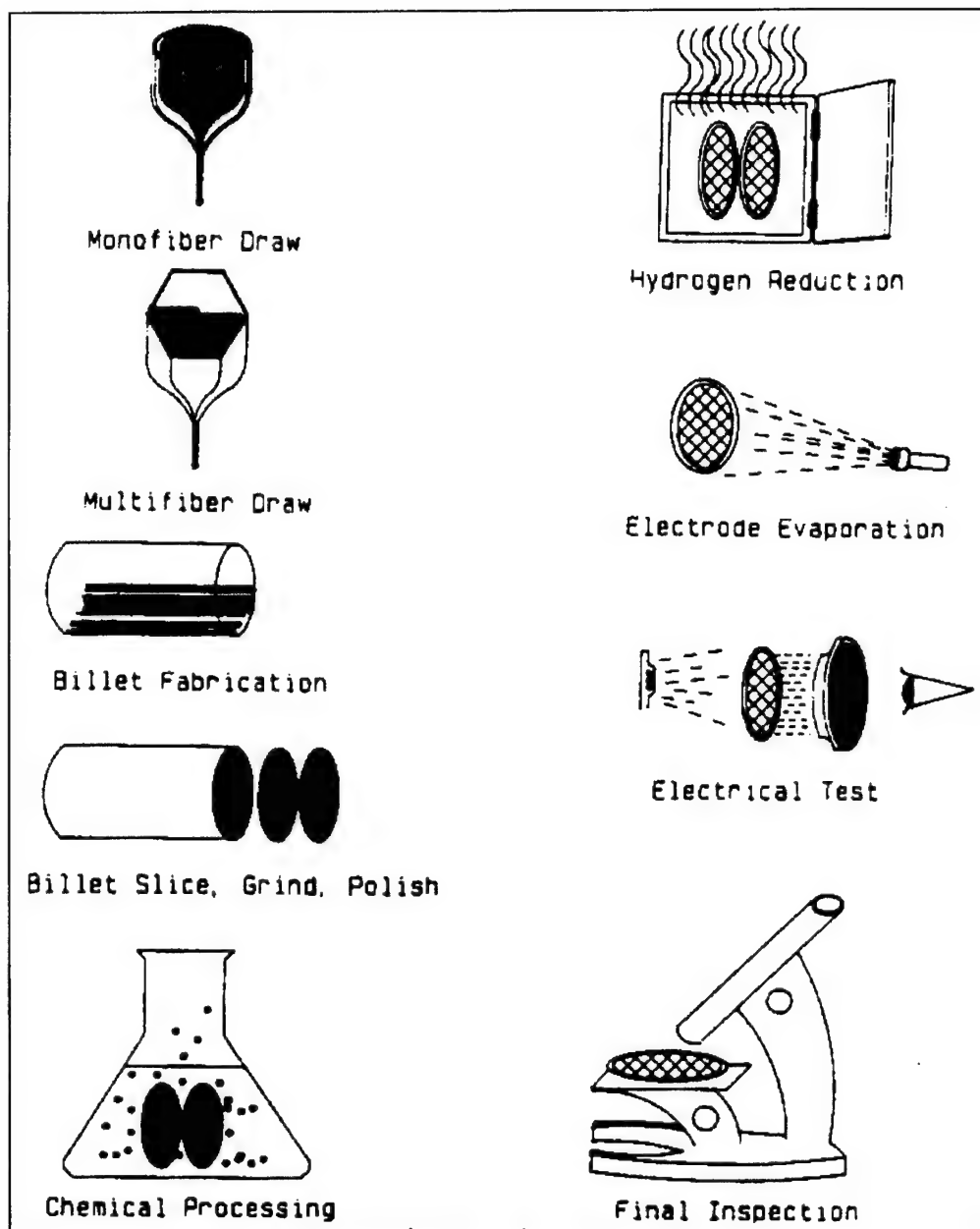
Figure 14: MCP Construction Process. Taken From Laprade (1989).

17

III. REVIEW OF PREVIOUS WORK

In 1990, a decision was made by the NPS Physics Department to study the detailed shape of the line profiles associated with the optically thick ionospheric emissions. This required an instrument with considerably higher spectral resolution than the instruments already in use. A search commenced for the appropriate instrument to meet this need. There are numerous descriptions in the literature of high resolution instrumentation that have been proposed and tested over the years. Since ionospheric studies are typically performed from sounding rockets, the space shuttle or orbiting satellites, the size of the instrument is of paramount importance. For many instruments, resolution is generally proportional to the size of the instrument. An interferometric device, on the other hand typically has a relatively compact size even with a very high resolution.

The range of wavelengths for ionospheric studies spans from the middle ultraviolet (MUV) to the extreme ultraviolet (EUV) regions. Regrettably, optical elements that have high transmittances are not available below 1200 Å. Therefore, only all-reflective instruments are suitable for the study of these ionospheric emissions. The search focused on an interferometric device with all-reflection optics. Several alternative designs are described below. The list is not all inclusive, but represents a sampling of the many designs available.

The Spatial Heterodyne Spectroscopy (SHS) Instrument [Bush, 1991] is a special class of the interference spectrometers. The instrument, shown in Figure 15, has no moving parts since mechanical scanning is not necessary. This removes the complexity normally associated with the scanning interferometers. Collimated light is incident upon the V-grove diffraction grating. Two opposite diffraction orders, (+1 and -1), are directed from the grating to the side mirrors. The beams are reflected to the opposite side mirror and back to the grating. In this way, one order travels clockwise around the system while
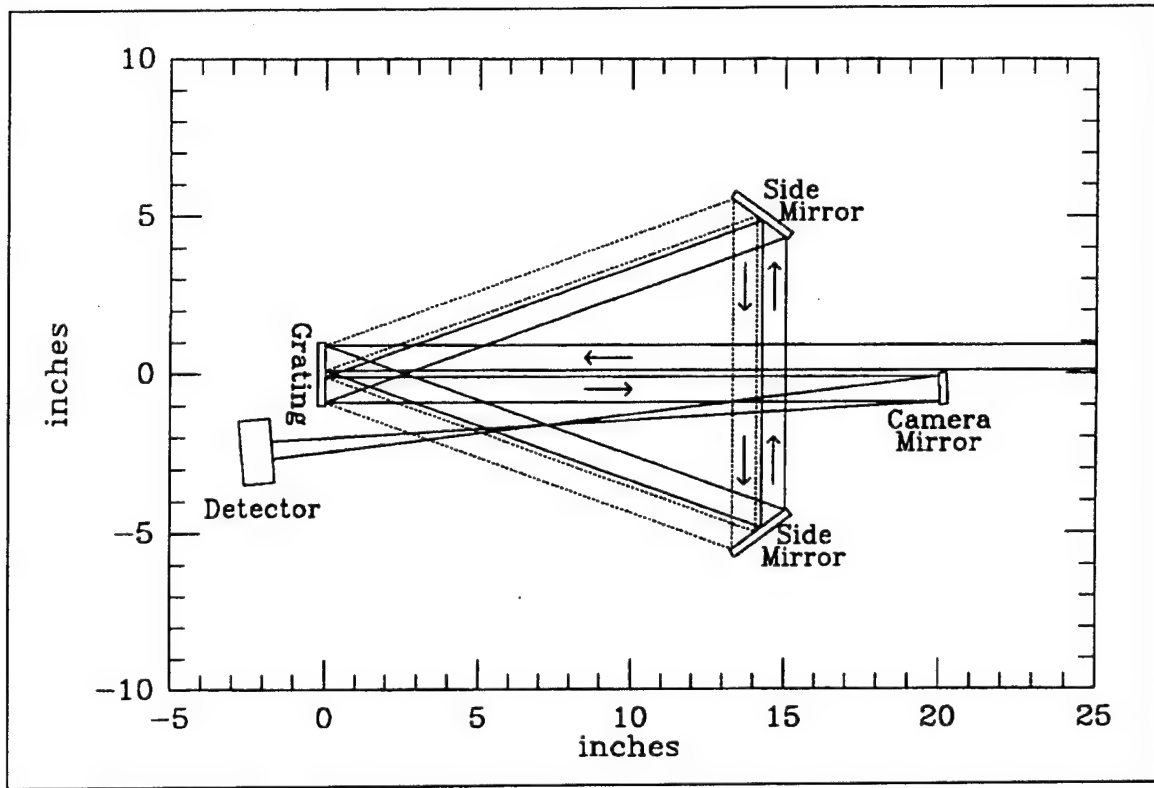
Figure 15: Layout of the All-Reflection SHS Interferometer. Taken From Bush, (1991).

the other order travels counterclockwise. At the grating, the two beams recombine and finally the light is focused by a concave camera mirror onto the detector for display. Both beams travel essentially the same path and reflect off the same optical elements making the instrument in insensitive to slight misalignments. For this reason, the instrument is described as self-compensating.

Another type of all-reflection interferometer, from Kruger (1972), is shown in Figure 16. Light passing through the lower half of the aperture S is collimated by the mirror M. The light is then split into two separate beams by the holographic grating G. Mirrors M_1 and M_2 reflect the beams back to the grating where they recombine. Mirror M focuses the image through the upper half of the aperture S onto the detector.
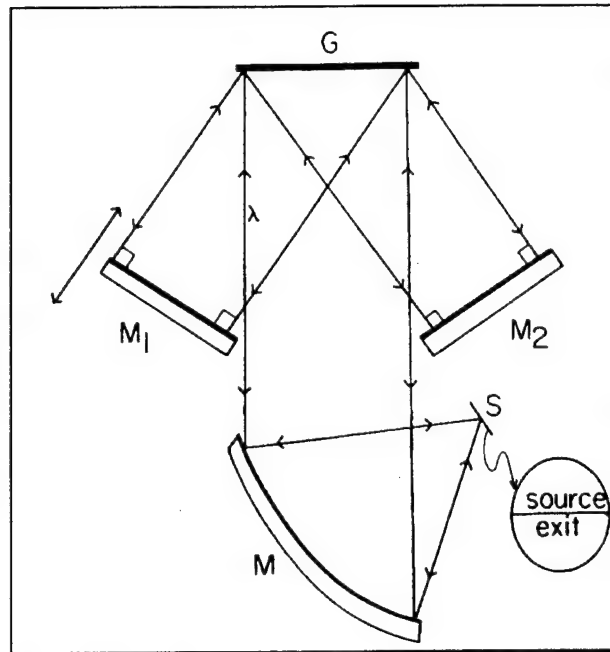
Figure 16: Layout of a Two-Beam Interferometer. Taken From Kruger, (1972).

Figure 17 is a variation of the two-beam interferometer shown in Figure 16 [Kruger, 1972].
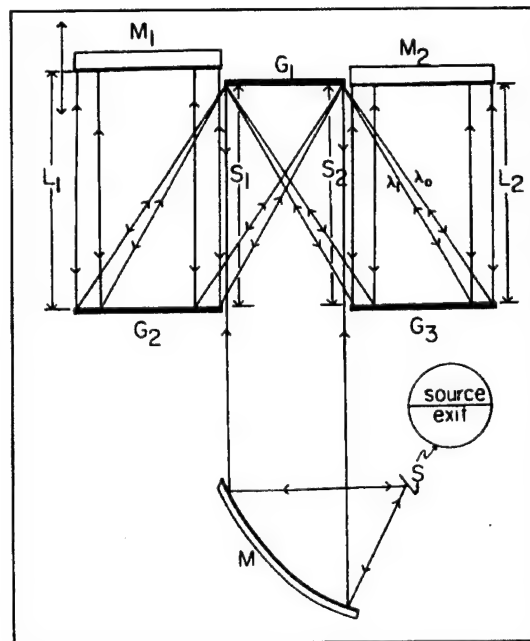
Figure 17: Layout of a Multiple Grating All-Reflection Interferometer. Taken From Kruger, (1972).

Incident light is collimated by mirror M and is directed to grating G_1. The light is diffracted into left and right beams which intercept gratings G_2 and G_3, respectively. These two gratings have the same groove frequency as grating G_1. In turn, G_2 and G_3 diffract their respective beams to mirrors M_1 and M_2. These mirrors cause the beams to be redirected back through the instrument. The image is formed at the exit aperture S.

In spite of the many all-reflection interferometers available for consideration, a different configuration was chosen for investigation at NPS. Design, development and testing of an interferometer that used a concave spherical grating in an off-plane Rowland circle configuration was undertaken by Nichols (1990). A schematic of this design is shown in Figure 18.
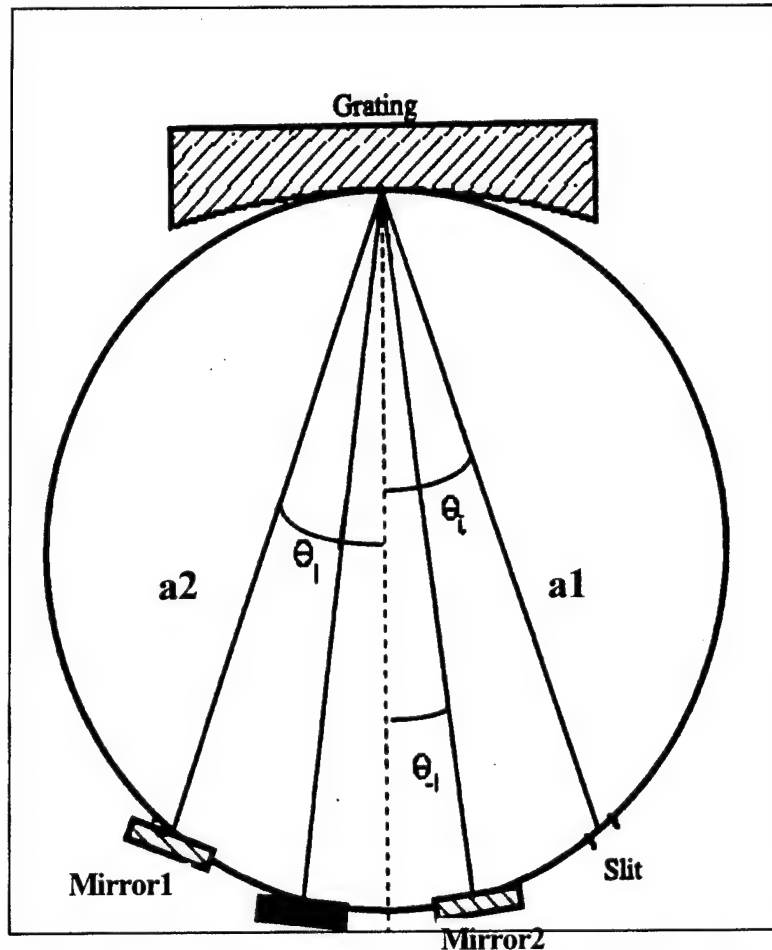
Figure 18: Rowland Circle Interferometer. Taken From Nichols, (1990).

Light enters at the slit and travels along the path a1 to the grating. There, the beam is diffracted into two beams, the 0 and +1 order beams. The 0 order diffraction beam travels along path a2 to Mirror1 where it is reflected back along the same path to the grating. At the grating, the beam undergoes a +1 order diffraction and is directed toward the detector. Conversely, the +1 order diffraction beam undergoes a similar process involving Mirror2. However, this time the +1 order beam returning to the grating undergoes a 0 order diffraction before being directed to the detector. Note, both beams have now undergone a 0 and +1 order diffraction. The detector was a CCD camera. A typical interference pattern from this instrument is shown in Figure 19. This pattern is elliptical as opposed to circular due to an astigmatism associated with the off-axis placement of the optical elements in the Rowland circle.
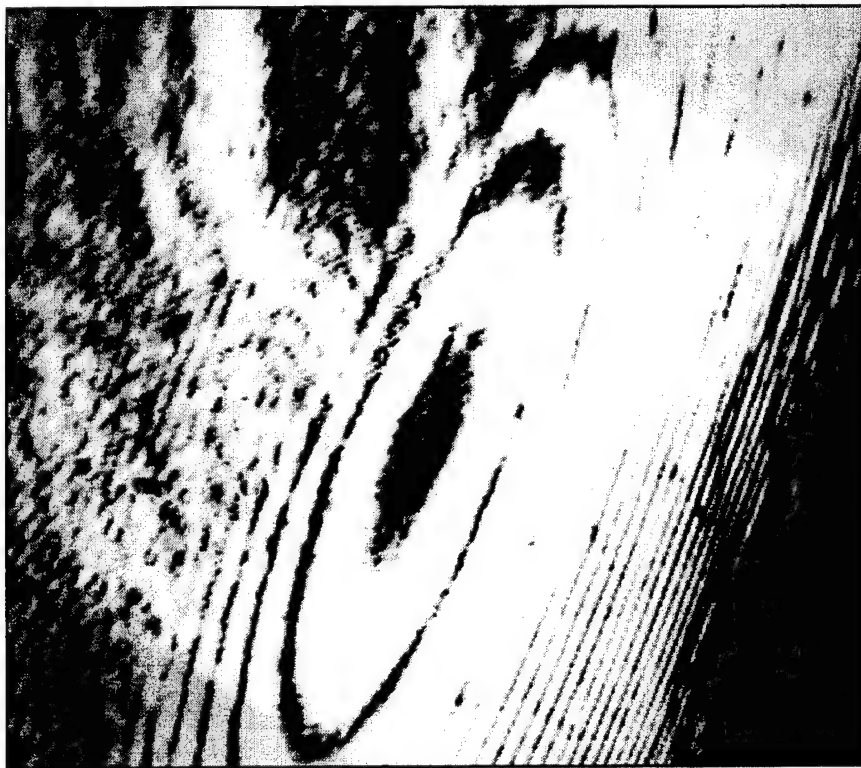
Figure 19: Interference Pattern for Rowland Circle Interferometer, He-Ne Laser, 5435 Angstrom. Taken From Nichols, (1990).

23

Overall, Nichols concluded that this design was simple, compact, and lightweight and the interference pattern was sufficiently stable for remote operations. He pointed out however that the astigmatism required more study.

A numerical analysis of the Rowland Circle Interferometer was performed by Wallace (1992). He modeled the interferometer using the Dudley Atkinson Ray Trace (DART) program [Atkinson, 1993] developed at the NPS. Wallace evaluated a number of configurations of the optical elements in an attempt to refine the design. He found that it was impossible to completely eliminate the astigmatic effects of the spherical grating. Due to the anticipated difficulty in the interpretation of the elliptical interference pattern, a decision was made to terminate the evaluation and development of this design.

Instead, Wallace began to investigate a new design for an all-reflection interferometer. This design, shown in Figure 20, was named the All-Reflection Michelson Interferometer (AMI). This stemmed from the fact that the basic operation of
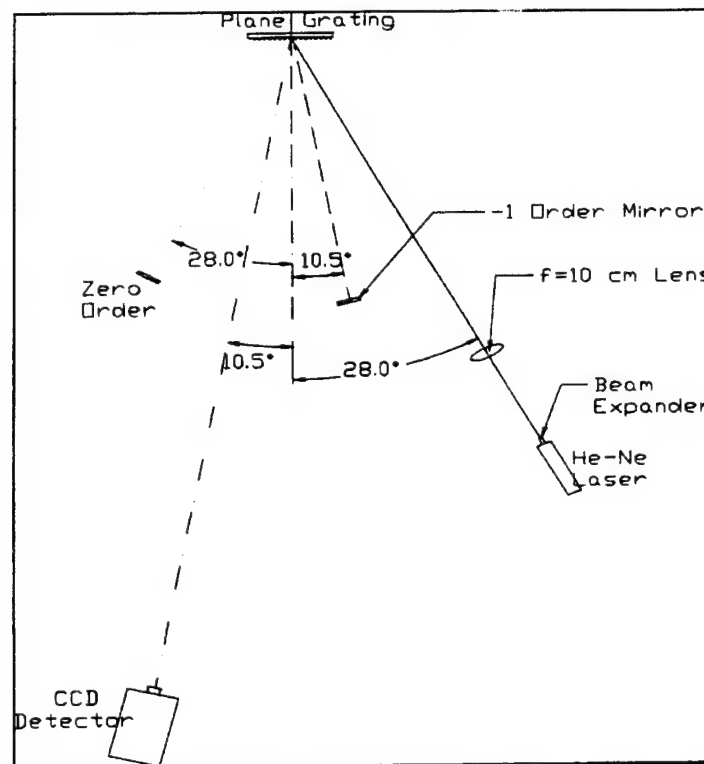
Figure 20: All-Reflection Michelson Interferometer. Taken From Wallace, (1992).

24

the instrument follows that of a Michelson Interferometer. The AMI used a planar holographic grating instead of a spherical grating in the Rowland Circle Interferometer. A planar grating offers the advantage of producing a linear interference pattern which is more amenable to Fourier Transform Analysis than the elliptical pattern of the Rowland Circle Interferometer.

As discussed in the Grating Theory section of the Background chapter, the layout of the optical elements depends on the incident angle of the light source to the grating and the operating wavelength. A collimated light beam is incident upon the grating and undergoes a 0 and a +1 order diffraction at prescribed angles. Using the 5435 Å He-Ne Laser, Wallace chose an incident angle of 28°. The grating equation dictates that the planar mirrors for the 0 and +1 order beams be placed at -28 and 10.5°, respectively. These mirrors reflect the 0 and +1 order beams back to the grating where they experience a +1 and a 0 order diffraction, respectively. As with the Rowland Circle Interferometer, both beams have now experienced a 0 and a +1 order diffraction. An interference pattern obtained by Wallace is shown in Figure 21. Wallace predicted the resolving power for this design, when operating in the EUV region, would be approximately 1×10^6.
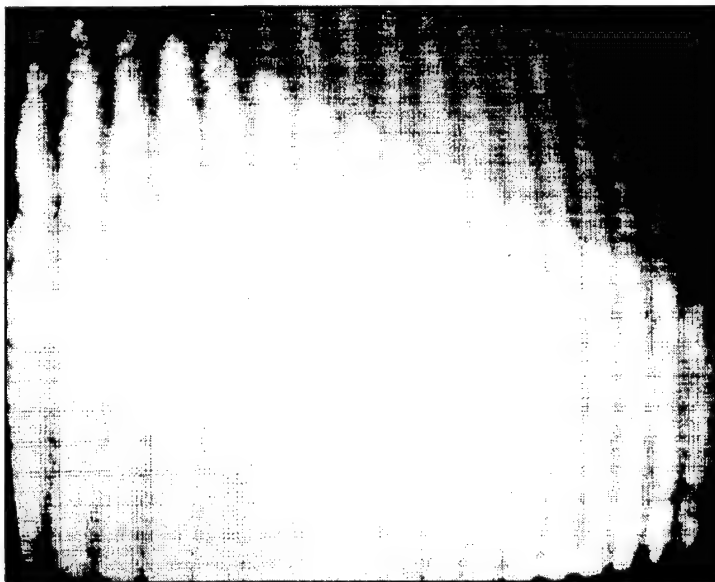
Figure 21: Interference Pattern, He-Ne Laser, 5435 Angstrom. Taken From Wallace, (1992).

Wallace's AMI design achieved superior results compared with the previous design, but several engineering problems were noted. The interference pattern was extremely susceptible to disruption from environmental vibrations. Thermal convection currents in the room, were sufficiently large to disturb the interference pattern as well. Additionally, the interference pattern was very sensitive to small angular adjustments of the reflecting mirrors. Accurate control of the mirror adjustments could not be obtained from the optical mount hardware used. Another hardware problem stemmed from the fact that the collimating element for the initial design was a lens. Since the ultimate goal is to use all-reflection optics, the lens must be replaced with an off-axis parabolic mirror as the collimator.

In order to understand the performance of the AMI, Carlson (1993) modeled the instrument using the DART ray tracing code. The ray trace analysis was performed for both the 5435 Å He-Ne Laser and the 1304 Å triplet oxygen emission. Carlson's analysis indicated that the AMI could be used effectively throughout the ultraviolet region especially in the EUV.

Concurrent with Carlson's numberical analysis, several engineering changes were performed by Risley, (1993). First, Risley addressed the issue of the collimator for the incident beam. In order to produce a collimated beam, he mounted a circular pinhole at the focus of an off-axis parabolic mirror. Verification of the beam's collimation was achieved by imaging the pinhole with a telescope focused at infinity. Next, Risley undertook the construction of an ultraviolet detector. The detector consisted of a microchannel plate image intensifier that was coupled to a linear photodiode array. Attempts to produce an interference pattern using an ultraviolet Mercury pen-ray lamp were unsuccessful.

Gill (1994) performed the second engineering redesign of the AMI. In this redesign, Gill considered the replacement or modification of the diffraction grating, the optical work bench and the ultraviolet detector. Gill proposed that for a given

wavelength there exists a minimum grating groove frequency for use in the AMI. A grating, with a groove frequency of greater than $2/(3\lambda)$, would eliminate all unwanted diffraction orders. As a result, Gill replaced the 1200 grooves/mm with a 2400 grooves/mm sinusoidal grating. Next, he mounted a low profile optical rail to an optical table with a vibration isolation base cushioned by nitrogen gas. This effectively prevented any environmental vibration source from reaching the instrument. Finally, the detector was replaced with a solid state CCD camera with computer interface. This allowed, for the first time, the images of the interference pattern to be saved directly to disk for later manipulation and analysis.

Gill first tested the AMI using a visible source. It may appear that this is a step backward from use of an ultraviolet source by Risley. It was a necessary step however since Risley was unsuccessful in achieving an interference pattern with the ultraviolet source and since major equipment changes had occurred. A bandpass filter was used to remove all wavelengths except the 5461 Å Mercury green line. Numerous interference patterns were recorded and subsequently analyzed using Fourier Transforms. This configuration produced the first reliable and repeatable interference pattern in the history the AMI. Since this initial testing had such favorable results, the instrument was tuned to the Sodium 5889 Å doublet. The resulting interference pattern and spectrum are shown in Figures 22 and 23. This spectrum is complicated by the fact that the tuned wavelength

Figure 22: Interference Pattern, Sodium Doublet, 5889 Angstrom, File Image32.TIF.
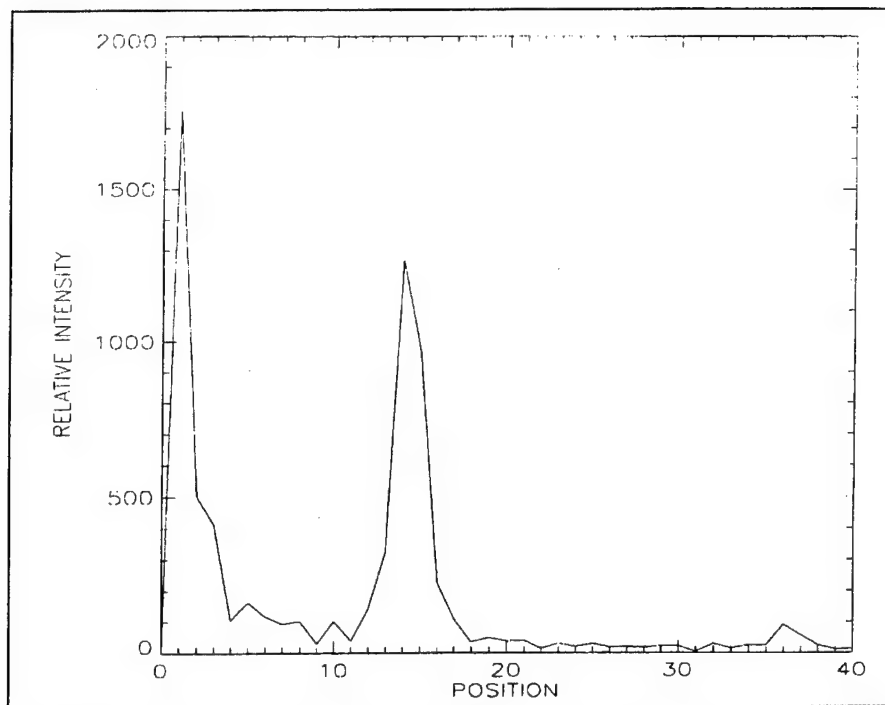
Figure 23: Spectrum, Sodium Doublet, 5889 Angstrom. Taken From Gill, (1994).

for the measurement is located between the two emission lines (Gill, 1994). However, the doublet lines can be seen at n=14 and n=36. The feature at n=1 is an artifact of the inversion process. Gill found that the relative intensity of the peaks varied depending upon the number of rows of data used for coaddition. This problem is discussed in much greater detail below in the Analysis Software chapter of this thesis. Finally, Gill configured the AMI for operation in the ultraviolet. This configuration change entailed realignment of the optical elements and coupling an ultraviolet image intensifier to the CCD detector. Initial testing using a 2537 Å Hg pen-ray lamp produced no interference pattern. It is at this point that the work for this thesis began.

IV. DEVELOPMENT OF THE MID-ULTRAVIOLET INTERFEROMETER

This chapter presents the development of the AMI during the past year and a half since Gill (1994). This research follows a progression through two major instrument design and development phases and a development period for the analysis software. Subsequently, the analysis of two different light sources for the Hg emission at 2537 Å was accomplished. A third design and development phase is currently underway.

The configuration of the AMI is outlined below to provide a starting point for the discussion of the research involved with this thesis. The research began with the instrument configured as shown in Figure 24. A pinhole was used as the field stop for
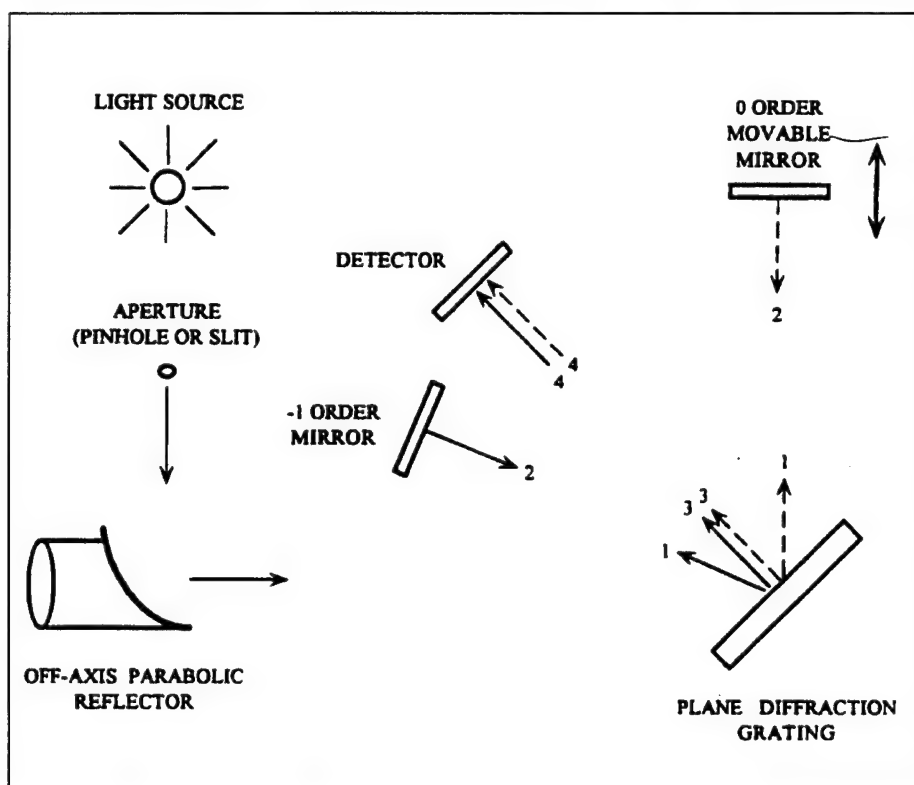
Figure 24: All-Reflection Michelson Interferometer Layout. Taken From Gill, (1994).

the Hg pen-ray lamp light source. This pinhole was located at the focus of an off-axis parabolic mirror which collimated the incident light. The collimated beam was directed at the grating with an incidence angle of 5°. The remaining optical components were aligned according to the grating equation. The detector consisted of an ITT image intensifier mounted directly to the front of the CCD chip in the Electrim Corporation CCD camera.

Gill (1994) suggested three possible causes for his failure to obtain an interference pattern using an ultraviolet source with this setup. These included overlapping of spectral orders, interference from other diffraction orders and intensity mismatch between the 0 and +1 order beams. Recommendations from Gill for the improvement of this instrument included:

1. Improvement of the collimating method for the incident light.
2. Optimization of the diffraction grating.
3. Reduction of the thermal and vibrational disturbances.
4. Development of a suitable detector for use throughout the ultraviolet region.
5. Development of a mirror mount that would allow a much finer adjustment of the interference pattern.

A. DESIGN AND DEVELOPMENT, FIRST ITERATION

In this design and development iteration, the main focus was to obtain an ultraviolet interference pattern. As a result, an investigation was launched to find ways to eliminate or mitigate the circumstances that prevented the formation of the pattern. Below is the description of that research.

1. Spectral Overlap and Interfering Orders

In order to investigate the possibility of overlapping spectral orders or interference between diffraction orders, one must consider the Hg spectrum in the region of 2537 Å.

An Hg spectrum, obtained from the NPS MUSTANG instrument by MacQuarrie [Private Conversation, 1994] is shown in Figure 25. The spectrum is for the region of 1850 Å to 3400 Å. There are four prominent emissions in this spectral range: the 2537, 2653, 2967 and the 3125 Å emissions. While the 2537 Å emission appears to be comparable in intensity to the other emissions, it is in fact several orders of magnitude more intense. The emission saturated the detector during the measurement of this spectrum. An investigation into whether the 2537 Å emission was subject to spectral order overlap or interfering orders was performed despite the apparent differences in the intensities of the other emissions.
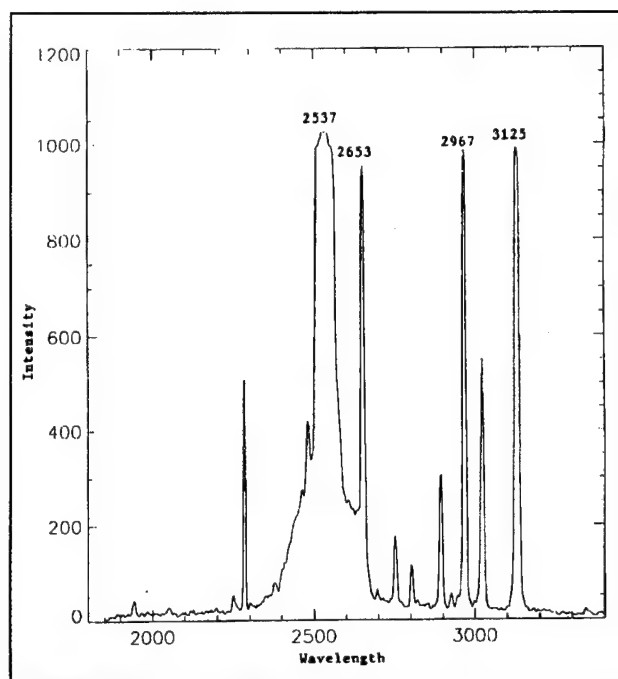
Figure 25: Mid-Ultraviolet Spectra of Pen-Ray Lamp Measured With MUSTANG Instrument [MacQuarrie Private Conversation, 1994].

In order to visualize the location of the beams of these wavelengths in the AMI, a graphical representation of the diffraction grating equation was developed. This representation is referred to as a diffraction map. In a diffraction map the independent variables are the order number, m, and the incident angle of the input. Therefore for a

31

given groove frequency and wavelength, the location of the m_{th} order beam can be located if the incident angle of the input beam is known.

The diffraction map in Figure 26 includes three families of curves. There is one family for the -1, +1 and +2 order beam sets. Within each family the 2537, 2653 and 2967 Å emissions are plotted. In this way, the location of the diffracted beams for each of the wavelengths can be visualized.
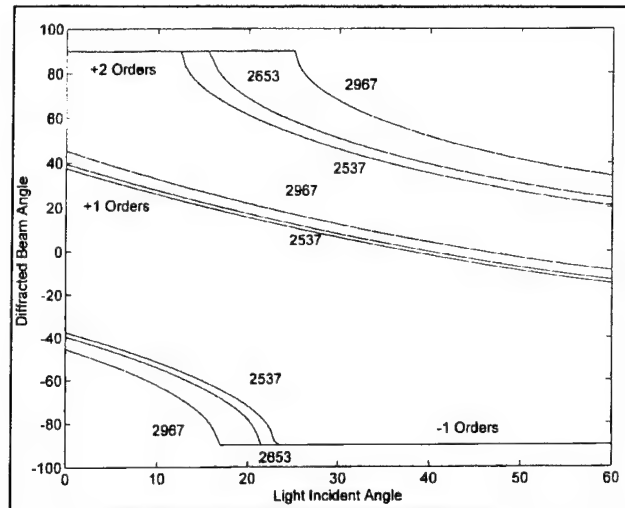
Figure 26: Diffraction Map, 2400 grooves/mm, 2537,2653 and 2967 Angstrom.

Figure 26 shows for example that the 2653 Å emission +1 order beam is in very close proximity to the 2537 Å beam. Finding the 2653 Å emission using the AMI proved to be very difficult. The detector gain had to be increased significantly above the level necessary to detect the 2537 Å emission. For this reason, interfering diffraction orders was eliminated from the possible causes of the failure to obtain an interference pattern.

As discussed in the Background chapter, overlapping spectral orders can occur when polychromatic light is incident upon a grating. Specifically, overlap can occur if the light contains a wavelength that is an integer fraction of the measured wavelength. Consider for example, the wavelength, 2537 Å, which undergoes a +1 order diffraction. If the inlet beam contains light at 1268.5 Å, then the +2 order beam at this wavelength will be coincident with the 2537 Å +1 order beam. Two solutions exist for this problem

32

in the current setup. First, the 1268.5 Å emission is a vacuum ultraviolet emission. This emission is present only in a vacuum since it is quickly absorbed at atmospheric pressure. Secondly, the spectral response of the image intensifier is limited to approximately 1800 - 3500 Å. The upper limit is due to the tail off of the quantum efficiency of the CsTe photocathode. The lower limit stems from the fact that the quartz input window of the image intensifier is opaque for wavelengths less than 1800 Å. This spectral response band eliminates the possibility of overlapping spectral lines for this design even if the AMI is operating in a vacuum.

2. Beam Intensity Differences

Concentrating on the differences in the intensities of the two order beams (0 and +1), another diffraction map was generated for the 2537 Å emission. In this map, six different curves corresponding to the incident beam, the -1, 0, +1 and +2 diffracted beams and the beam incident upon the detector are represented. Figure 27 shows this diffraction map for a sinusoidal grating with a groove frequency of 2400 grooves/mm. From the map, it can be seen that for an incident angle 5° the possible diffraction beams include the -1, 0 and +1 orders. Alternatively, only the +2, +1 and 0 order beams are observed for an incident angle of 45°.
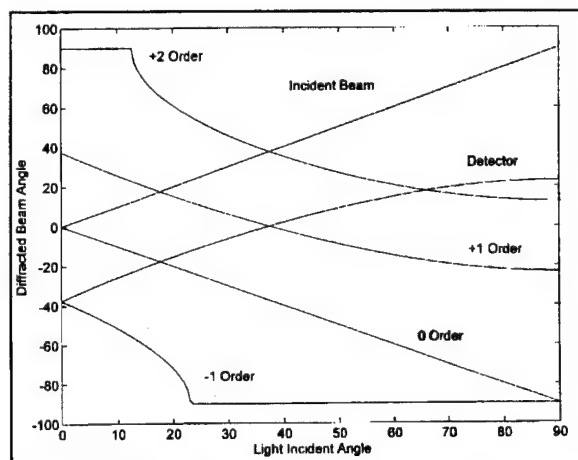
Figure 27: Diffraction Map, 2400 grooves/mm, 2537 Angstrom.

33

For the 5° incident angle setup, it was observed that more of the beam's energy was diffracted out of the 0 order beam. This makes the +1 order beam of higher intensity than the 0 order for that setup. Conversely, for the 45° incident angle setup, the 0 order is of higher intensity than the +1. This was verified by configuring the instrument for various incident angle setups. Measurement of both the 0 and +1 order beam intensities were performed by blocking out the opposing order mirror and observing the intensity of the remaining order with the detector. After many iterations, the incident angle of 15° was chosen in an attempt to equalize the beam's intensities. The configuration template using the incident angle of 15° is shown in Figure 28. Here, the inlet beam is diffracted into the 0 and +1 order beams at -15° and 20.5° to the grating normal, respectively. The beams, reflected back to the grating, are diffracted to the detector at 20.5°. Measurement of the beam intensities for this setup indicated that the beams were nearly equal.
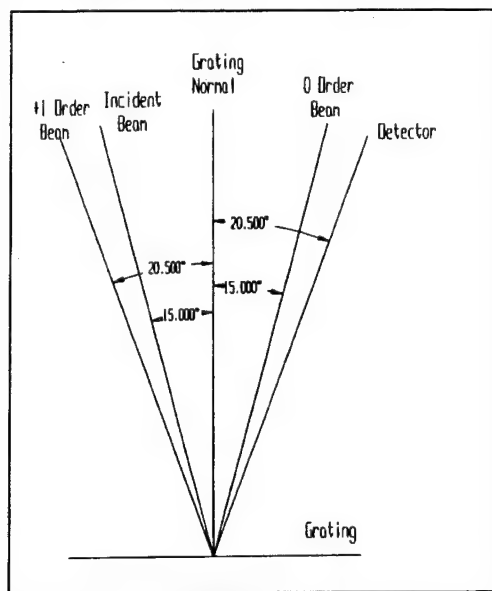
Figure 28: Configuration Template for AMI, 2400 grooves/mm, 2537 Angstrom, Incident Angle = 15°.

3. Results of the First Iteration

Having measured each beam individually, both beams were then allowed to reach the detector. After a progression of adjustments, the first interference pattern for this

instrument using an ultraviolet source was observed and recorded. Figure 29 shows a representative interference pattern recorded by the instrument in this iteration. The pattern contains five interference fringes albeit with relatively low modulation. This interference pattern was a major breakthrough in the development of the AMI. Equalizing the beam intensities proved to be the dominant factor in this success. The AMI could easily and repeatedly create an ultraviolet interference pattern.

Figure 29: Interference Pattern, Pen-Ray Lamp, 2537 Angstrom.

In spite of this breakthrough in the design of the AMI, several issues were noted in the instrument's operation and with the interference pattern it produced. Manual adjustment of the +1 order mirror to change the spatial frequency of the interferogram proved difficult. The slightest movement of the adjustment screw by hand was much more than was needed for fine tuning. The low modulation of the interference pattern was attributed to two effects. First, the low modulation of the interference pattern is attributed to the inability to completely match the intensities two beams. The net result is a reduction in the difference between the intensity of the peaks and valleys. Next, the blurring of the interference pattern is due to the method in which the image intensifier is coupled to the CCD chip. This produced a low detector modulation transfer function (MTF) and hence, the images produced by the detector are low quality. The combination of these effects resulted in a very limited range of observable spatial frequencies. A maximum of only about six fringes could be observed.

35

B. DESIGN AND DEVELOPMENT, SECOND ITERATION

The interferogram obtained from an ultraviolet source demonstrated the capability of the AMI to operate in the ultraviolet. An analysis of the results suggested that several modifications were needed to improve the AMI. This includes rework of the diffraction grating, the mirrors and their mounts and the ultraviolet sensitive detector. The following section contains a description of this work.

1. Diffraction Grating

Analysis of the diffraction map for the AMI suggested that the maximum beam intensity would occur in a configuration where only the two desired orders exist. It was further hoped that at this configuration the two beam's intensity would be nearly equal. As seen in Figure 27, there is no incident angle that satisfies this condition for a 2400 grooves/mm grating. The -1 order beam is present for incident angles of 0 to 23° whereas the +2 order beam is present for all incident angles greater than 13°. For this reason, a diffraction grating with a higher groove frequency was needed. It was suggested by Gill (1994) that there is a minimum groove frequency for a given wavelength that satisfies this condition. This minimum groove frequency is given by $2/(3\Sigma)$. For the 2537 Å emission, this corresponds to a groove frequency of at least 2630 grooves/mm. The 2400 grooves/mm grating used during the first iteration did not satisfy this condition. As a result, a higher groove frequency grating was sought. Conversations with the technical representatives at Milton Roy Grating Laboratory provided information regarding suitable commercially available gratings. After comparing the diffraction maps for the available gratings, a 3600 grooves/mm sinusoidal grating was chosen. Figure 30 shows a diffraction map for the 3600 grooves/mm grating. As shown in this figure, the grating has a relatively large range of incident angles where only the two desired beams exist. This is consistent with Gill's minimum groove frequency grating suggestion. However, an optimum grating cannot be found without considering the desired geometry of the

36

optical components. For compactness, it was found that the desired geometry has the detector located between the 0 and the +1 order mirrors. Additionally, for mechanical reasons equal spacing between the optical components is desired. Based on Figure 30, the optimal configuration using these criteria occurs near an incident angle of 40°. The
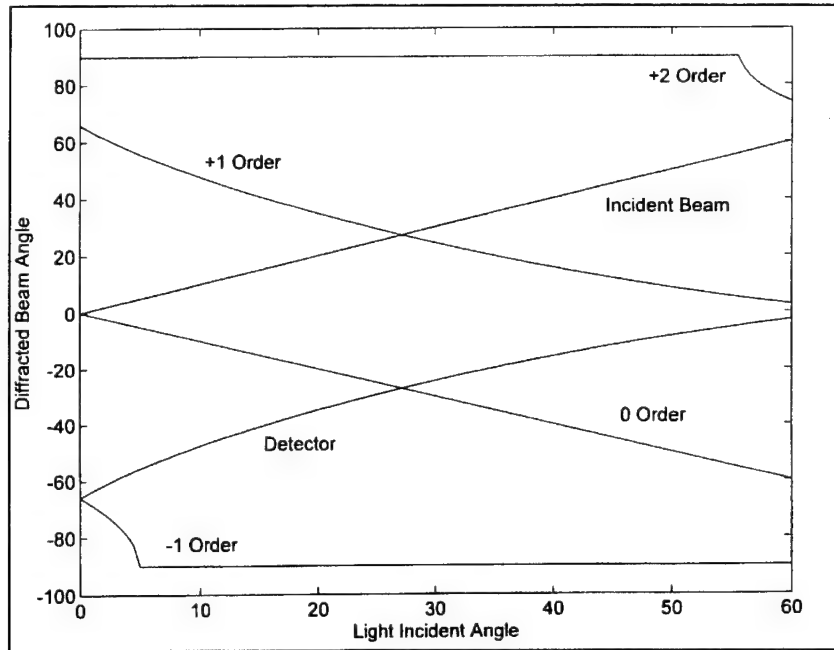
Figure 30: Diffraction Map, 3600 grooves/mm, 2537 Angstrom.

resulting configuration template is shown in Figure 31. All angles are measured relative to the grating normal.

Based on the template, a summary of the beam paths is as follows: For an incident angle of 40°, the inlet beam is split into two diffraction orders. The 0 and +1 order beams are diffracted at -40 and 15.696° respectively. The 0 and +1 order beams are reflected back to the grating by planar mirrors. At the grating, the 0 order beam acts as another incident beam at 40°. It undergoes a +1 order diffraction at 15.696°. Similarly, the +1 order beam undergoes a 0 order diffraction at -15.696°. At the detector, both beams have undergone a 0 and a +1 order diffraction and are coincident to the detector to form an interference pattern.

37
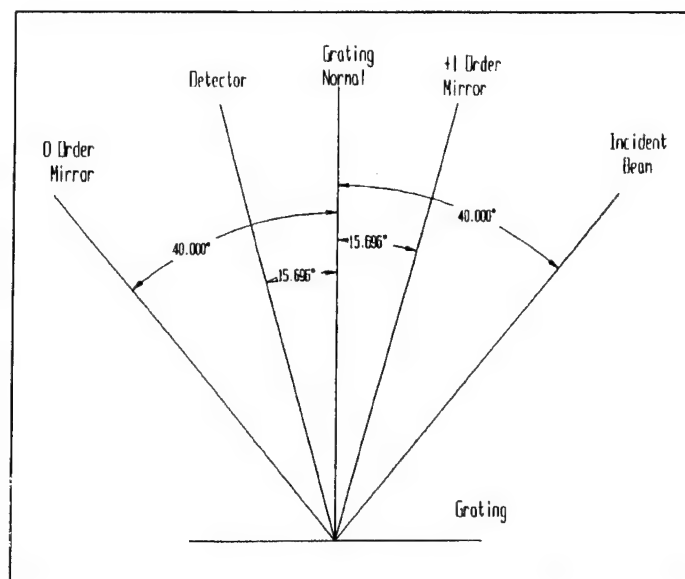
Figure 31: Configuration Template for AMI, 3600 grooves/mm, 2537 Angstrom, Incident Angle = 40°.

2. Mirror Selection

After the completion of the diffraction grating analysis, an investigation of the mirrors used in the first iteration revealed two major deficiencies. First, the mirrors were silver coated mirrors that were intended for reflecting visible or infrared light. At wavelengths less than 4000 Å, the reflectivity of silver drops to less than 10 percent. Recall that each beam undergoes three reflections before reaching the detector, excluding the grating. If the reflectivity of each mirror is 10 percent, over 99.9% of the incident light is lost at the mirrors alone. An aluminum mirror with a MgF_2 coating has a reflectivity of greater than 80 percent. In this case, the amount of light lost would be less than 50 percent. It was also found that the accuracy of the surface finish for the mirrors was unacceptable. The mirrors used in the first iteration were standard lab grade mirrors with a surface finish accuracy of approximately λ to $\lambda/3$ (based on the standard reference wavelength of 6330 Å). To reduce the dispersion of the reflected beam to an acceptable level, a surface accuracy of greater than $\lambda/10$ was required. Two new planar mirrors with

a surface accuracy of λ /10 were obtained from JML Direct. Additionally, an off-axis parabolic mirror and precision mount was obtained from Space Optics Research Lab (SORL). The surface accuracy of this collimator was λ /15. The mirrors and collimator were aluminum coated with MgF_2 for increased reflectance.

3. Ultraviolet Sensitive Detector

It was decided that a redesign of the detector was also necessary for the second iteration. As separate components, the image intensifier and the CCD computer camera, operated as desired. However, the combination of the two resulted in a low MTF. This low MTF is directly related to the method used to couple the intensifier to the CCD chip. The image intensifier was literally bolted to the front of the camera so that the fiber-optic output of the intensifier touched the CCD chip's glass input window. No index matching gel or other coupling technique was used. As a result, the interference pattern was blurred. Another consequence of the detector mounting was that only a square portion, measuring 8 mm by 8 mm, of the 25 mm diameter fiber-optic output was used. This represented a dramatic loss of data. Figure 32 shows on a relative scale the mapping of the image intensifier onto the CCD detector. Notice that most of the image is not recorded by the CCD.
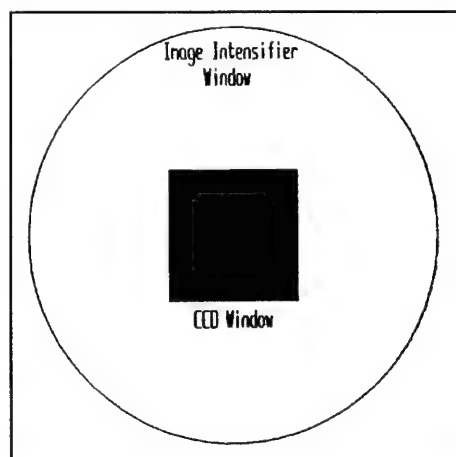
Figure 32: CCD Coverage of Image Intensifier Output Window.

39

To resolve this problem, a fiber-optic taper was used to reduce the image size from the image intensifier to match the CCD chip input window. Figure 33 shows the mapping of the image intensifier onto the CCD using this fiber-optic taper. The glass input window of the CCD chip was also replaced with a fiber-optic window. To complete the coupling, index matching gel was used at all interfaces. Electro-Optical Services was contracted to procure the fiber-optic taper and couple the image intensifier to the CCD chip in a single housing.
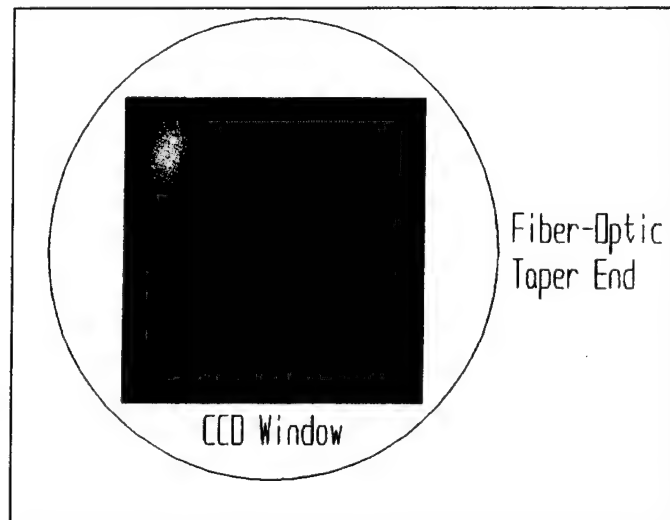
Figure 33: Fiber Optic Taper Coverage of CCD Window.

4. Fine Adjustment Mirror Mounts

The final change of the second iteration involved the mirror mounts. To allow much finer adjustment of the mirrors, a new mirror mount system was needed. New Focus, the manufacturer of the mirror mounts used in the first iteration, markets a Pico Motor drive controlled mount. This mount not only matches the currently used mounts, but provides a capability for a minimum screw turn of 2 milliradians or approximately 0.12°. An additional benefit of this mount was its ability to remotely adjust the mirror without disturbing the instrument setup.

40

All optical elements were lowered so that their optical centers were 3.5 inches above the optical bench. This reduced the susceptibility of the instrument to thermal and vibrational disturbances. It also demonstrated that the design could conform to compact size requirements.

5. Summary of the Second Iteration Changes

To summarize, the components obtained for the second iteration include:

1. A 2-inch square 3600 grooves/mm sinusoidal grating with a MgF_2 coating.

2. Two one-inch planar aluminum mirrors with a surface finish accuracy of $\lambda/10$ and a MgF_2 coating.

3. A 2-inch aluminum off-axis parabolic mirror with a surface finish accuracy $\lambda/15$ and a MgF_2 coating.

4. Image Intensifier fiber-optically coupled to the CCD camera.

5. Pico Motor drive controlled one-inch optical mount with controller.

In essence, the instrument was completely rebuilt from bench up.

6. AMI Reconstruction

With all components in hand, the process of reconstructing the instrument began. A template showing the positions of the optical elements, similar to Figure 31, was used. This template facilitated the placement of the elements onto the optical bench. Although the alignment of the collimator and the 150 μm pinhole seems to be a trivial task, the procedure is rather involved. First, a lighted reticule telescope focused at infinity was aligned to the optical bench to provide a reference for the collimated beam. The telescope axis was adjusted to make it parallel to the mounting holes in the bench making other component installation easier. Next, the collimator and the pinhole were placed in their approximate positions. The collimator mount has an optical reference flat for use in the alignment. The lighted reticule of the telescope acts as a source of light that is reflected

41

back to the telescope by the reference flat. The mirror is aligned with the telescope when the image of the reticule is superimposed on the real reticule. The telescope is then shifted to place it in the beam of the collimator. The focus of the collimator can then be found by imaging the pinhole back through the collimator. Since the telescope is focused at infinity, the pinhole will appear to be a point source when it is at the focus of the collimator. When the pinhole is not at the focus, its image is distorted. Using an iterative process, the pinhole is brought into focus. With this alignment complete, the alignment of the grating was undertaken. The grating was mounted so as to place it in the center of the collimated beam and at the origin of the configuration template. An alignment is performed to ensure that the grating grooves are perpendicular to the surface of the bench. To do this, a flat plate with a small aperature was placed in the collimated beam to restrict its size. By measuring the height of the two diffracted beams, an iterative process of adjusting the tilt and rotational alignment of the grating was performed. With the alignment of the pinhole/collimator set and grating complete, the remainder of the instrument lineup was performed. This step, of course, is wavelength dependent. Recall that the template shown in Figure 31 provides a reference for positioning the +1 and 0 order mirrors and the detector for a 2537 Å emission. After the +1 and 0 order mirrors were mounted to the bench per the template, the distance between each of two mirrors and the grating were made equal. A flat disk was machined to fit over the grating for protection during these measurements. A hole drilled in the disk's center provided the reference point for the measurement. The other reference point was located just below the optical center of each mirror mount. First, the distance to the +1 order mirror from the grating was measured using an inside micrometer. Next, the distance from the grating to the 0 order mirror was adjusted, using a micrometer-adjusted translation stage, to make it equal to the +1 order distance. The flat reference disk was then removed from the grating. The detector was also placed according the template ensuring that the detector barrel face was perpendicular to the line extending from the grating on the template.

42

Before adjusting the mirror alignment, the flat plate with the aperature was again used to restrict the beams size. The individual mirror alignment was accomplished by blocking one mirror and adjusting the other to center the restricted beam onto the middle of the detector screen. The procedure was repeated for the other mirror. With alignment of the instrument complete, the flat plate was removed from the collimated beam and the second iteration instrument was then ready for testing. With only minor adjustment, the instrument produced a clearer interference pattern with higher modulation. Also the pattern was much easier to fine tune. A typical pattern is shown in Figure 34.
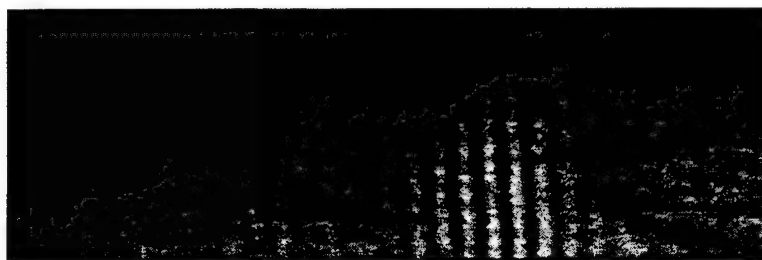
Figure 34: Early Second Iteration Interference Pattern, Pen-Ray Lamp, 2537 Angstrom, File 19Feb4.TIF.

Note, a closer look at the fringes reveals a slight tilt to the pattern. Correction of this tilt is one of several steps performed by the data reduction software. This software is described in the next chapter.

V. DEVELOPMENT OF DATA-REDUCTION SOFTWARE

With the design and development of the second iteration complete, the task of developing the data-reduction software for the instrument began. The programming can be broken down into two major areas. The first area involves the generation of a one-dimensional interferogram from a two-dimensional interference pattern. To do this, data must be read from a TIFF file and coherently added. The second area of programming is the Fast-Fourier Transform (FFT) algorithm. This algorithm creates a double-sided, symmetric interferogram from the one-dimensional interferogram and performs a FFT to obtain the desired spectrum. These procedures are discussed in detail in the sections below. The data-reduction software consists of one main program, SPECTRA2.PRO, and two subroutines, IMAGE.PRO and DELTA3.PRO. The listing for these programs can be found in the Appendix.

A. GENERATION OF THE 1-DIMENSIONAL INTERFEROGRAM

The first half of the data-reduction software generates a one-dimensional interferogram. Recall that each interference pattern is stored in a file using TIFF file format. The name of the TIFF file is used as an input to the subroutine IMAGE.PRO. In this subroutine, specialized Interactive Data Language (IDL) commands open the TIFF file and read the data in as a matrix with the variable name IMAGE. Since the CCD chip in the Electrim Camera has a 753x244 pixel array, the variable IMAGE is a 753x244 matrix. The subroutine returns IMAGE to the main program for processing.

The matrix IMAGE is used as an input for the next subroutine, DELTA3.PRO. This subroutine calculates the phase error for each row. This phase error is due to a tilt in the interference pattern. Row 122 is used as the reference row and its phase error is assumed to be zero. Since the reference row was chosen in the middle of the matrix, it is necessary to perform the comparison from row 121 up to row zero and again from row

45

123 down to row 243. To ensure that an empty row is not used, the sum of each row was compared with zero and skipped if necessary. To calculate the phase error, a correlation of the test and reference rows is performed. One can perform this procedure in either the spatial domain or the frequency (Fourier) domain. The results are the same regardless of the method used. Since the correlation in the spatial domain involves the convolution of the reference and test rows, it is computationally intensive. For this reason, performing the correlation in the frequency domain was chosen. A correlation in the frequency domain requires the Fourier Transform of the reference and test rows to be taken. The correlation is then found by multiplying these transformed rows and taking the Inverse Fourier Transform. To find the phase correction necessary for the row the peak in the correlation must be found. To do this, a peak finding algorithm is used. If the rows were perfectly aligned, the correlation would be maximum at zero spatial frequency. If the maximum is not at zero spatial frequency, the location of the peak pinpoints the value of the phase correction. The value of the phase correction is stored in the array DEL at the corresponding location for that row. This comparison is repeated for each row and the resulting array DEL is returned to the main program.

Once the phase correction for each row is known, the rows are horizontally shifted to the correct phase. Again, this phase correction could be accomplished in either the spatial or frequency domain. For the reasons given above, it is much easier to this correction in the frequency domain. After obtaining the Fourier Transform of the individual rows in the matrix IMAGE, each row is multiplied by a complex phase shift corresponding to its respective value in the DEL array. The Inverse Fourier Transform returns the corrected row. This is stored in the corresponding row of a new matrix COMP.

To improve the signal-to-noise ratio, the rows of the phase corrected matrix COMP are all added to form a one-dimensional array. The resulting array has 753 elements compared to the COMP matrix's 753x244 elements. This array is commonly

46

known as an interferogram. The interferogram has a large nonzero DC offset that varies with position. Removal of this offset is necessary to analyze the data. This is accomplished by taking the derivative of the interferogram [Davis, 1976]. After the DC offset is removed, the one-dimensional interferogram is stored in the array DAT1.

B. FAST-FOURIER TRANSFORM ALGORITHM

There are two standard configurations for the recorded interference pattern. The interference pattern is either double-sided or single-sided depending on the location of the zero path difference (ZPD) point. The ZPD point is defined as the point where the two beams (the 0 and +1 orders) recombine with a zero phase difference, Λ. Recall from Figure 5 that this results in a maximum in the interferogram. If this maximum is located in the center of the interference pattern, the resulting interferogram is referred to as double-sided. In this case, the interferogram is symmetric about the ZPD point. If the ZPD point is moved to the side of the interference pattern, a single-sided interferogram is generated. The single-sided interferogram measures a greater optical path difference than the double-sided interferogram. As a result, the single-sided interferogram produces a higher resolution spectrum. However, for computational purposes a double-sided array is desired because it eliminates the complex phase issues associated with single-sided interferograms.

We have chosen to use a technique that combines the advantages of single- and double-sided interferograms by artificially creating a doubled-sided interferogram from the single-sided interferogram. First, a peak finding algorithm is used to find the maximum of an interferogram. As stated above, this maximum corresponds to the zero path difference point. In general, the ZPD point will not be centered precisely on a pixel. If not corrected, the off-pixel location of the ZPD would result in an asymmetric interferogram which would introduce a phase error into the resulting spectrum. As before, shifting the ZPD point is easier in the frequency domain. After completion of this

47

shift, the ZPD point will be located on an integer pixel number. Since the ZPD point is known, the interferogram is simply reversed to create the opposite side of the symmetric interferogram. The resulting double-sided, symmetric interferogram is stored in the array DAT. The desired spectrum is obtained by taking the FFT of DAT. The real component of this transform contains the final spectrum. One criterion of a correctly processed spectrum is that the imaginary component of the FFT be negligibly small compared to the real component. Finally, the spectrum is stored in the array SPEC. For informational purposes, the number of points used in the single-sided interferogram is recorded in the first element of the SPEC array.

VI. RESULTS

With the completion of the instrument design and setup for the 2537 Å emission and data-reduction software, the instrument was ready for evaluation. An ORIEL mercury (Hg) pen-ray lamp was initially used as a test light source. The hyperfine structure of this emission, produced by the different mercury isotopes, provides a useful reference for determining the instrument's resolution. After a thirty minute warm-up period for the lamp, the instrument was ready for testing. The interference pattern was easily found on the first try. Before the interference pattern was analyzed, the characteristics of the instrument were investigated and documented.

A. INSTRUMENT EVALUATION

Several significant improvements over the first iteration were noted. The vibration isolation system on the optical table drastically reduced the vibrational disturbances on the pattern. A similar but smaller reduction was noted for the thermal disturbances and air convection currents as a result of lower the optical mounts. The use of a cardboard box to completely cover the instrument eliminated any remaining disturbances to the interference pattern. The modifications to the ultraviolet detector resulted in a drastic increase in the MTF. A clear image of an interference pattern, similar to the one shown in Figure 35, could now be generated. The number of fringes that could be observed approached two hundred. This is an increase in performance of approximately thirty fold from the first iteration. Furthermore, the small angular displacements of the mirror, made possible by the Pico Motor, enabled very fine adjustment of an interference pattern. The number of fringes or spatial frequency in the pattern could now be changed by less than one fringe per adjustment. This control

49

enabled an interference pattern to be adjusted to any spatial frequency, numbering from one to over two hundred.
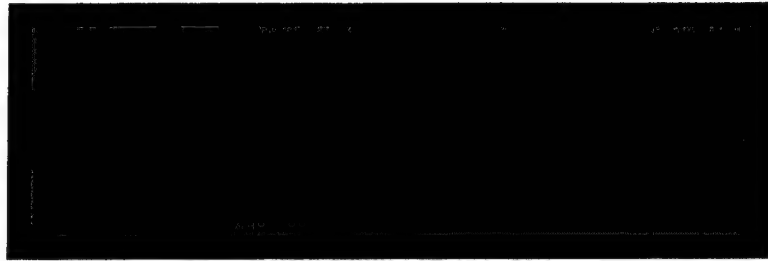
Figure 35: Interference Pattern, Pen-Ray Lamp, 2537 Angstrom, File WU2.TIF.

An analysis of the modulation of the interference patterns as a function spatial frequency was made to determine the optimum operating point. To do this, a Hg interference pattern was recorded for a range of spatial frequencies. The corresponding spectra were calculated using the data-reduction software described in Chapter 5 and are plotted in Figure 36. This figure shows that the modulation intensity increases with
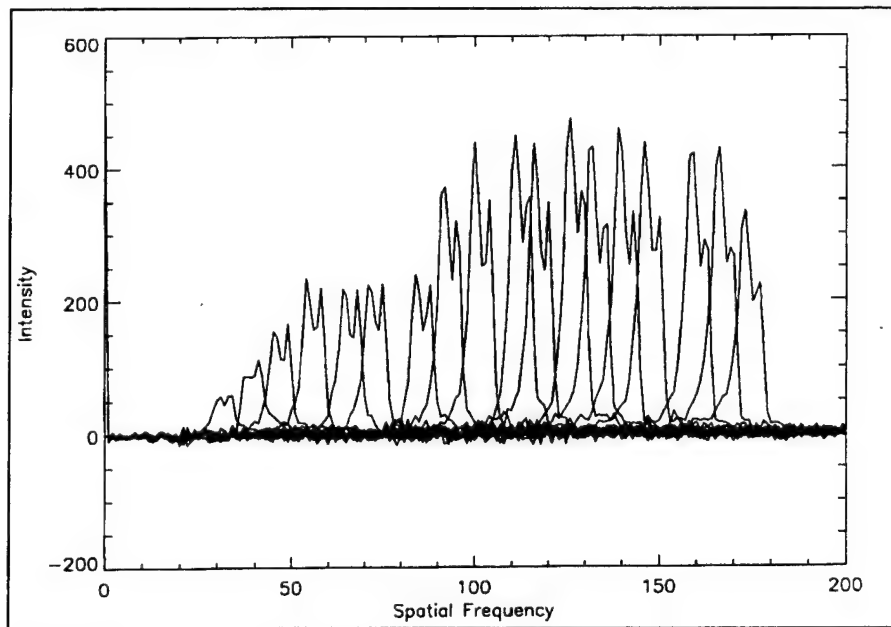
Figure 36: Overplot of Spectra With Increasing Spatial Frequency, Files 19Feb3.TIF Through 19Feb20.TIF.

increasing spatial frequency to a maximum at a spatial frequency of approximately one hundred and twenty five. The trend then reverses and the modulation intensity lowers with increasing spatial frequency. The fall off at high spatial frequencies is probably due to the finite size of the pin-hole and the associated angular spread of the collimated beam. A full explanation of this trend is still needed. These results suggest the preferred operating range of spatial frequencies is from approximately one hundred to one hundred and fifty fringes.

The tilt of the interference pattern can be changed by adjusting the angular position of the +1 order mirror with respect to the horizontal axis in the plane of the mirror. The Pico-Motor controlled mount enables one to visually align the fringe pattern tilt while it is observed realtime on the computer monitor. This alignment need only be approximate since the exact vertical alignment is achieved in the phase correction section of the data-reduction software. As discussed in the Data-reduction Software Development Chapter, the desired interference pattern has the ZPD positioned to one side of the detector. Since the path lengths of the 0 and +1 order beams were initially equal, the ZPD point was initially located near the center of the pattern. By adjusting the translation stage of the zero order mirror, the ZPD location can be changed as desired. The amount of adjustment to relocate the ZPD from centerline to either side was approximately six millimeters.

B. ANALYSIS OF MERCURY PEN-RAY LAMP

With the evaluation of the interferometer complete, the data obtained from the AMI were ready to be analyzed. A typical interference pattern for the pen-ray lamp at 2537 Å is shown above in Figure 35. The coadded interferogram created by the data-reduction software is shown in Figure 37.

51
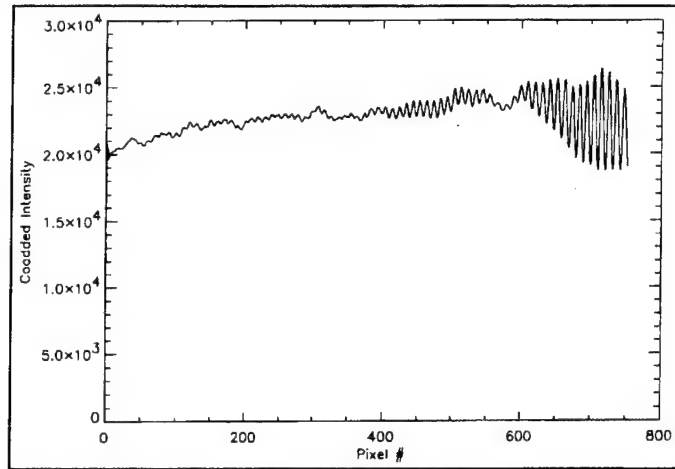
Figure 37: Coadded Interferogram, Pen-Ray Lamp, 2537 Angstrom.

In order to remove the varying DC offset from this interferogram, one takes its derivative. The results are shown in Figure 38.
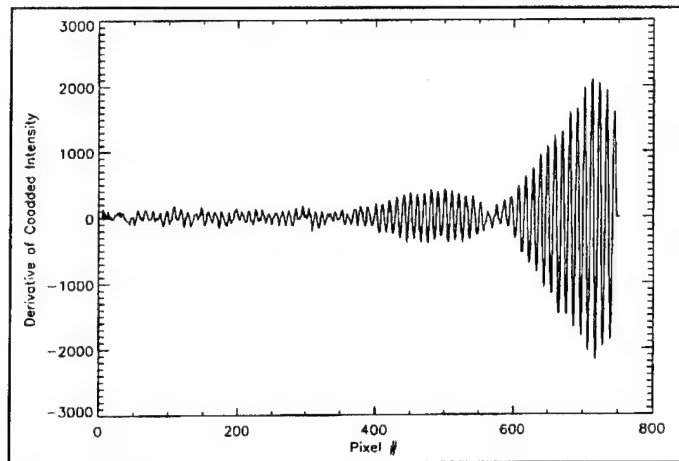
Figure 38: Single-Sided Interferogram, Pen-Ray Lamp, 2537 Angstrom.

From this single-sided interferogram, the software creates the double-side interferogram shown in Figure 39.

52
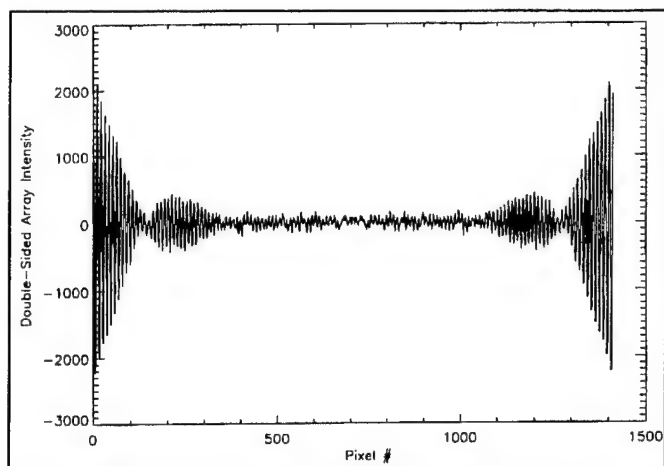
Figure 39: Double-Sided Interferogram, Pen-Ray Lamp, 2537 Angstrom.

The spectrum for the 2537 Å Hg emission from the pen-ray is found taking the Fast Fourier Transform of this array. A portion of the spectrum is shown in Figure 40. The x-axis corresponds to the spatial frequency of the interferogram, but can be interpreted as a relative wavelength.
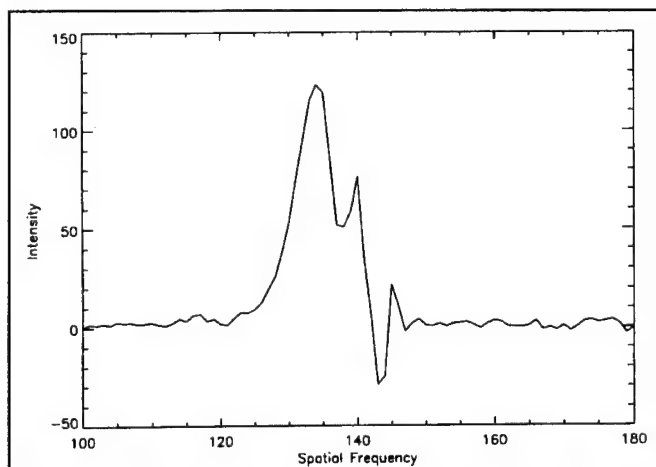
Figure 40: Spectrum, Pen-Ray Lamp, 2537 Angstrom.

In order to understand this emission, a high resolution spectrum of the pen-ray lamp had to be known. Scientists at the National Institute of Standards and Technology (NIST) were able to supply a copy of a spectrum for the ORIEL lamp measured by a

53

Chelsea Fourier Transform Spectrometer (FTS). The Chelsea FTS has a resolution of 1×10^6 at this wavelength. Figure 41 shows the spectrum at high resolution. This spectrum reveals a very broad and complex emission containing five components with a self-reversal dip in the middle of each line.
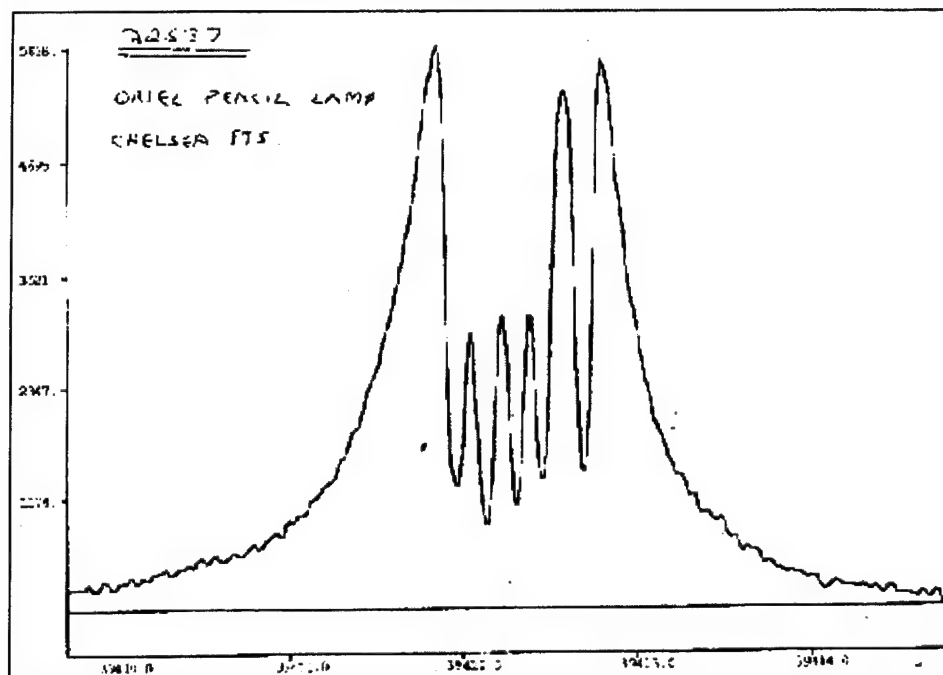
Figure 41: Chelsea FTS Spectrum, Pen-Ray Lamp, 2537 Angstrom Obtained From NIST, (1995).

It appears from the comparison of Figures 40 and 41 that the second iteration AMI lacks the resolving power to discriminate the emission lines from a pen-ray lamp.

C. ANALYSIS OF MERCURY GERMICIDAL LAMP

For additional testing , a new source was purchased to replace the pen-ray lamp. The pen-ray lamp spectrum is composed of five emissions that are each optically thick and therefore self reversed and very broad. The emissions in a germicidal lamp, on the other hand are optically thin and as a result are very narrow lines. In principle, the

54

germicidal lamp should produce a different interferogram. However, since the resolution of the AMI has not changed the hyperfine emissions will not be resolved.

Since the wavelengths for both sources are identical, no configuration change to the AMI was necessary. After a nominal thirty minute warm-up period for the lamp, an interference pattern, similar to the one shown in Figure 42, was recorded.

Figure 42: Interference Pattern, Germicidal Lamp, 2537 Angstrom, File 19Feb2.TIF.

For this particular pattern, the ZPD point is located to the left side of the pattern. As before, this was accomplished by adjusting the 0 order mirror. As with the pen-ray lamp, the pattern was manipulated in order to phase correct and coherently add, remove the DC offset, create a double-sided interferogram and analyze the data to obtain the spectrum using the Fast Fourier Transform Algorithm. These steps are shown in the following sequence of figures. Figure 43 shows the coadded interferogram resulting from the data-reduction of Figure 42.
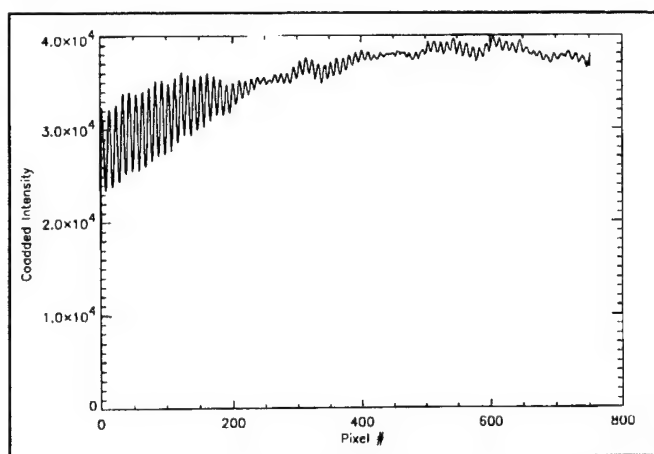
Figure 43: Coadded Interferogram, Germicidal Lamp, 2537 Angstrom.

55

Figure 44 shows the single-sided interferogram created after the derivative is taken to remove the DC offset.
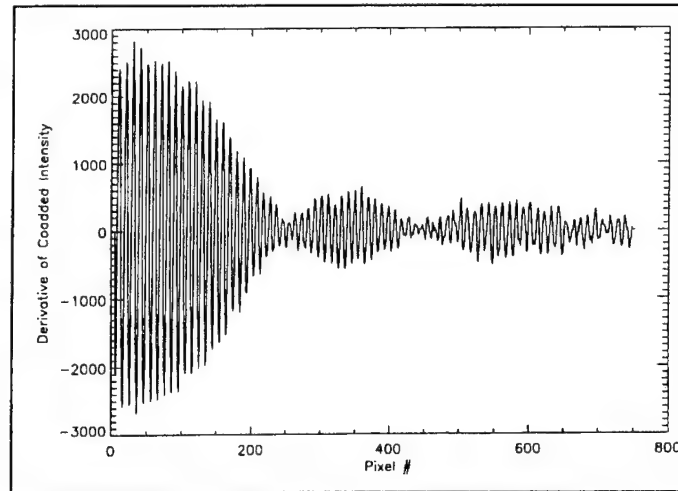
Figure 44: Single-Sided Interferogram, Germicidal Lamp, 2537 Angstrom.

Figure 45 is the resulting double-sided interferogram used for analysis in the FFT Algorithm.
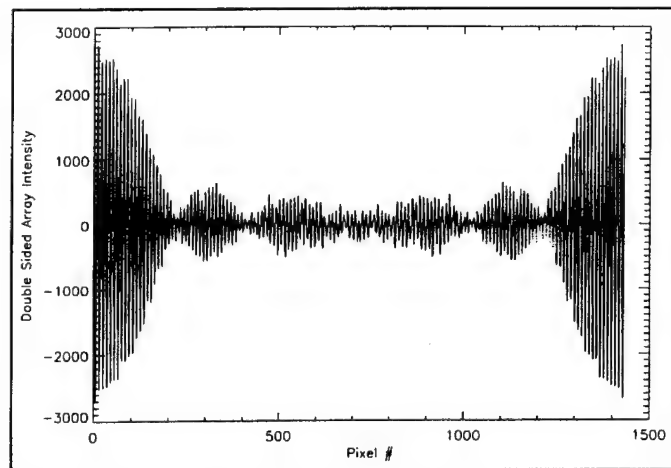
Figure 45: Double-Sided Interferogram, Germicidal Lamp, 2537 Angstrom.

The spectrum for the germicidal lamp is shown in Figure 46.

56
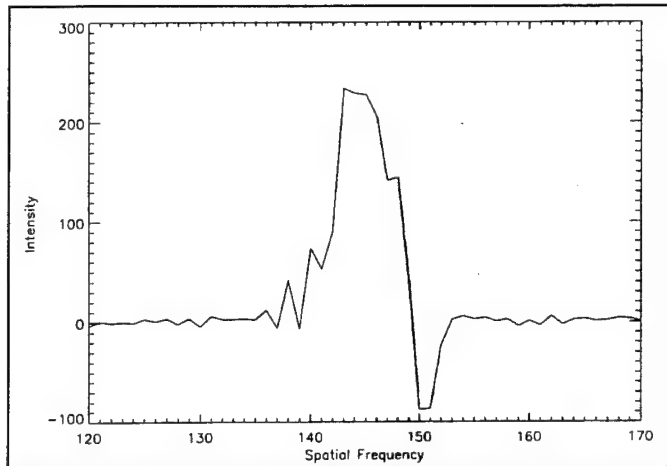
Figure 46: Spectrum, Germicidal Lamp, 2537 Angstrom.

Comparison of the results from the two sources reveals two noticably different interference patterns for the same wavelength emission. As predicted, the germicidal lamp produced a much wider interference pattern which can be seen by comparing Figure 44 and Figure 39. Both spectra contain negative spikes that are uncharacteristic of the results. One possible cause for this problem is that the interferogram is being sampled at irregular intervals. This is known as sampling error. The possible causes and correction of this difficulty are explored in the following chapter.

VII. PROPOSED DESIGN AND DEVELOPMENT, THIRD ITERATION

With the completion of the analysis for the pen-ray and germicidal lamps, the next iteration in the development of the AMI was set into motion. The two goals for the third iteration are:

1. Redesign of the instrument to increase the resolution.
2. Correction or mitigation of the sampling error.

The means to achieve these goals are discussed individually below.

A. INCREASING RESOLUTION

One method of increasing the resolution of the AMI is to increase the total optical path distance (OPD) of the interference pattern. This process involves capturing more of the interference pattern with the image intensifier and then recording more of the pattern with the CCD detector. Although this seems like a trivial statement, the process of capturing and recording more of the interference pattern is complicated and must be considered separately. Another method of increasing the resolution is to increase the groove frequency of the grating used in the AMI.

1. Increasing the Total Optical Path Difference

In order to capture more of the interference pattern a wider beam must propagate through the instrument and be detected by the detector. Several optical elements used in the second iteration limited the beam size to 1 inch. The diffraction grating and the collimator were not limiting and would in fact allow a beam size of up to two inches. The limitation of the beam size was dictated by the 1-inch diameter planar mirrors. In order to increase the beam size to two inches, new 2-inch mirrors and mirror mounts are required. To replace the 0 order mirror assembly, a 2-inch gimbaled mount would

suffice. However, to replace the +1 order mirror assembly a 2-inch Pico Motor driven gimbaled mount is needed. Recall the Pico Motor drive is necessary for the fine adjustment of an interference pattern. Both of these items are available from New Focus, Inc. To replace the actual mirrors, a set of high quality, precision ground mirrors is needed in a 2-inch diameter format. Aluminum mirrors with a surface accuracy of $\lambda/20$ and a MgF_2 coating are available from SORL.

In order to capture the 2-inch beam generated by these mirrors, the detector must also be changed. The detector used for the second iteration has only a 1-inch image intensifier input window. Hence, an image intensifier with a 2-inch input window must be used to match the 2-inch input beam. Since ultimately it is planned to operate the AMI throughout the ultraviolet region, this is a good opportunity to select the proper image intensifier for the job. The input window for the new image intensifier should be made of MgF_2 which is transparent down to approximately 1000 Å. Measurements at wavelengths shorter than this will require an image intensifier with no input window which is commonly referred to as bare windowed. The photocathode coating should be Rubidium Telluride (RbTe) to provide the best overall spectral response or quantum efficiency in the ultraviolet region for wavelengths greater than 1000 Å. A suitable image intensifier can be obtained through Ziemer and Associates, a distributor for DEP Delft Instruments.

2. Recording More of the Interference Pattern

The amount of data recorded by the CCD can be optimized by changing the coupling method between the image intensifier and the CCD input window. Recall from Figure 33 that the second iteration fiber-optic taper over fills the CCD input window. As a result, approximately thirty percent of the intensified image is unused. One can change the detector coupling so that the intensifier output is inscribed within the CCD input window as shown in Figure 47. In this manner, the maximum OPD of interference

pattern in the horizontal direction can be recorded by the detector. We have chosen to accomplish this coupling using a coupling lens device. This device could have the added
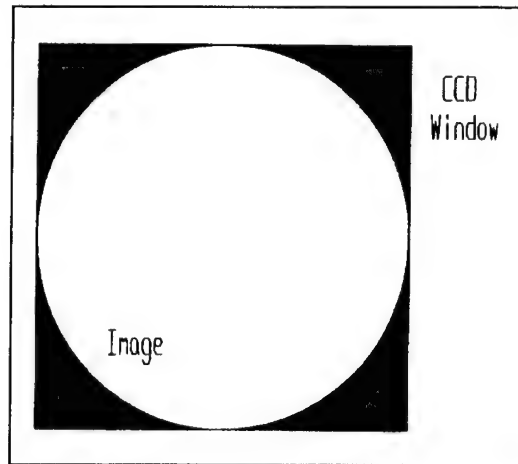
Figure 47: Coverage of CCD Input Window by the Image From the Lens Coupling Device.

benefit of eliminating any distortion introduced into the interference pattern during the demagnification process in the fiber-optic taper. After both modifications are made to the detector, the instrument throughput would be dramatically improved.

3. Higher Groove Frequency Grating

Another modification to the AMI which would result in an increase in resolution is to replace the current 3600 grooves/mm grating with one having a higher groove frequency. For a given wavelength, a higher groove frequency produces a greater difference in the wavefront tilt. This in turn produces a greater difference in the fringe spatial frequency. Milton Roy Company's highest commercially available groove frequency is 4260 grooves/mm. It should be noted that a grating with a groove frequency of greater than 6000 grooves/mm is desired for the AMI configured for emissions in the EUV. A grating with these groove frequencies can be developed but requires a long lead time and is therefore more expensive. Figure 48 shows a diffraction map for a 4260 grooves/mm grating. For maximum beam intensities only two diffraction beams are

desired. This is not a problem for this grating since there is no incident angle where more than two beams exist. Recall the desired geometry of the AMI has the detector located
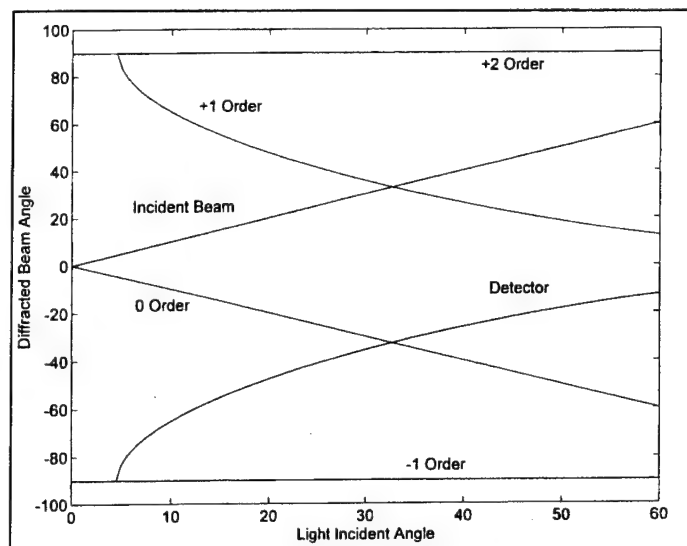
Figure 48: Diffraction Map, 4260 grooves/mm, 2537 Angstrom.

between the 0 and +1 order mirrors with equal distances between the components. To accomplish these two considerations, an incident beam angle of 45° is recommended. The corresponding configuration template is shown in Figure 49.
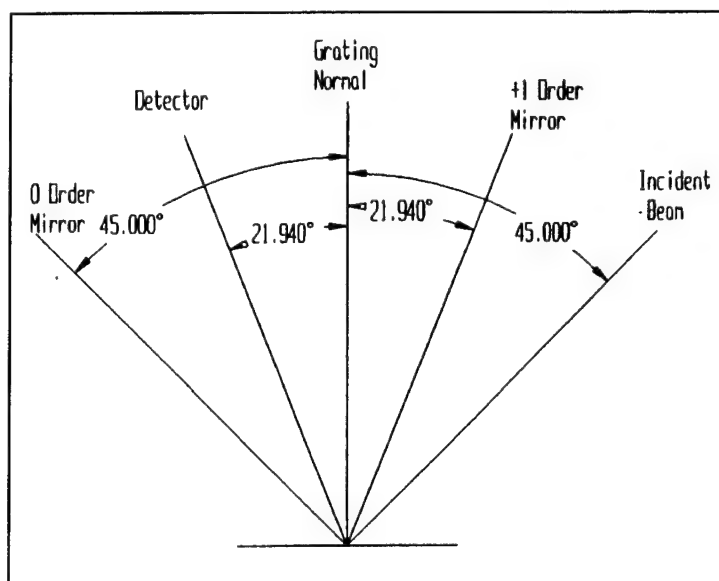
Figure 49: Configuration Template for AMI, 4260 grooves/mm, 2537 Angstrom, Incident Angle = 45°.

B. REPLACING THE LIGHT SOURCE

Recall that a narrow-emission light source is needed to understand, among other things, the possibility of a detector sampling error. A good candidate for this is the 2537 Å emission of Hg-198. Hg-198 has just one isotope and therefore only one emission line. This emission is present in other lamps but is masked by one or more emissions from the other isotopes of Hg. A Hg-198 electrodeless discharge lamp system should produce a narrow-emission line that is more than sufficient. An electrodeless discharge lamp system is desired because it produces a more stable emission than an arc lamp. The construction of such a lamp was described by Wolf (1978). This lamp system uses a quartz bulb filled with Hg. The bulb is housed in a specially designed microwave cavity that produces an electric field which excites the Hg atoms. The emission occurs when these atoms decay to their ground state. Another benefit of this system is the ease of switching between sources since the microwave exciter is a common component. A new bulb, selected for a desired spectral line, simply replaces the previous bulb in the microwave cavity. A variety of electrodeless discharge lamp systems are marketed by Fusion Systems Corporation.

C. SAMPLING ERROR CORRECTION

In order to correct or mitigate the sampling error, the first two development items must be completed. The possible causes of the sampling error include distortion of the interference pattern by the demagnification of the fiber-optic taper and beam distortion from the uneven mirror surfaces. By modifying the detector to include a lens coupling assembly vice a fiber-optic taper, the first explanation could be evaluated. Replacement of the 1-inch mirrors with the high surface accuracy 2-inch mirrors would shed light on the second possible cause. If replacing the mirrors and modifying the detector does not correct the sampling error, then a diagnostic interferogram is needed to investigate the sampling error. Replacing the source with the electrodeless discharge lamp system using

the Hg-198 bulb provides such a diagnostic interferogram. If a cause for this error cannot be located, this interferogram will also assist in the design of software to correct for the problem prior to data reduction.

D. THIRD ITERATION STATUS

The goals of the third design and development iteration for the AMI are to increase the instrument resolution and correct a possible sampling error found in the interferogram. As shown above, each of these items involves many aspects of the AMI's design. To accomplish these goals, changes must be made in the instrument's equipment, configuration and data reduction. The setup and data reduction changes are secondary to the equipment changes and cannot be implemented until after equipment procurement is complete. In summary, the following items are necessary for the continued development of the AMI:

1. Two 2-inch in diameter, MgF_2 coating planar mirrors with a $\lambda/20$ surface accuracy.

2. Two 2-inch, gimbaled mirror mounts with one manual driven and one Pico Motor driven.

3. An image intensifier with a 2-inch input window and a RbT coated photocathode.

4. A lens coupling device to couple the new 2-inch image intensifier to the CCD input window.

5. A 4260 grooves/mm sinusoidal grating coated with MgF_2.

6. An electrodeless discharge lamp system with a Hg-198 bulb.

Due to budgetary constraints, the procurement of the above items has not been completed. As a result, the third iteration is left for follow-on work.

VIII. SUMMARY AND RECOMMENDATIONS

A. SUMMARY OF EXPERIMENTAL RESULTS

The main objectives of this thesis were the continued development of the All-Reflection Michelson Interferometer and to extend its operation into the middle-ultraviolet wavelength range. The final design was required to have high resolution, be highly sensitive to low intensity emissions and be suitable for operations in space. This last requirement forces physical constraints on the instrument in that it must be compact, lightweight and economically constructed.

Previously, a prototype AMI was designed and operated using an incoherent visible light source. However, attempts to operate the instrument in the middle-ultraviolet region were unsuccessful. During the course of this research, it was found that a difference in the intensities of the 0 and +1 order beams was the major factor that prevented the formation of an interference pattern. To correct this problem, the prototype AMI underwent the first of three design and development iterations. A configuration was found where the beam intensities were nearly matched. This configuration resulted in the first interference pattern to be observed and recorded using an ultraviolet light source for the AMI.

Shortcomings of the first iteration AMI necessitated a ground-up redesign of the instrument. For this second iteration, the silvered mirrors were replaced with high surface accuracy aluminum mirrors that were coated with MgF_2 for increased reflectivity. To allow greater adjustment control, the +1 order mirror mount was replaced with a Pico Motor controlled mount. A 3600 groove/mm sinusoidal grating was used to ensure only two order beams were present and that their intensities were nearly matched. To increase the size of interferogram that was recorded and to increase the detector MTF, the image intensifier was fiber-optically coupled to the CCD detector. These changes produced clear interference patterns with high modulation of fringes intensities.

With the second iteration complete, data-reduction software was developed. In order to coherently add the interference pattern, its rows must be phase corrected to remove any fringe tilt. Next, the DC offset is removed by taking the derivative of the coadded interferogram. This is necessary due to the variation of the DC offset with detector position. A double-sided interferogram is created and the resulting spectrum is found using Fourier Transform techniques.

The AMI was tested using two different Mercury light sources, a pen-ray lamp and a germicidal lamp, for the same 2537 Å emission. The hyperfine lines of this emission provide a useful reference for determining the instrument's resolution. Although the AMI lacked the resolution for the second iteration to resolve these hyperfine lines, valuable information was gained from the two distinctly different interference patterns. The results of the data-reduction software suggest there is a sampling error associated with the detector. This is believed to be caused by imperfections in the detectors fiber-optic taper.

B. RECOMMENDATIONS FOR FUTURE STUDIES

In order to increase the resolution and correct the sampling error, a third iteration AMI has been proposed. To increase the resolution, the following changes are necessary: increase the total optical path difference across the face of the image intensifier, record more of the interference pattern with the CCD detector, and replace the grating with one having a higher groove frequency. It is believed that the above changes will correct the sampling error as described in the Sampling Error Correction section of the previous chapter. If not, a simplified interference pattern created by the new Hg-198 electrodeless discharge lamp will facilitate the development of sample error correcting software. None of these 'third iteration' recommendations have been completed due to lack of funding. It is hoped that the continued development of this promising instrument will begin early in 1996 and a prototype flight instrument will be constructed later in the same year.

APPENDIX

```
PRO SPECTRA2,FILE,SPEC


;*******************************************************
;**   Contains qualifying statements necessary for    **
;**   program.                                         **
;*******************************************************
  COMP=COMPLEXARR(753,244)
; WHANNING=SHIFT(HANNING(753,ALPHA=.5),376)
  WHANNING=1

;*******************************************************
;**   Calls the IMAGE.PRO program inputing the file   **
;**   name for export and returning the matrix IMAGE  **
;**   that contains the interference pattern to be     **
;**   evaluated.                                       **
;*******************************************************
  IMAGE,FILE,IMAGE

;*******************************************************
;**   Calls the DELTA3.PRO program inputing the matrix**
;**   IMAGE.  DELTA3.PRO finds the horizontal          **
;**   displacement of the lines with respect to a      **
;**   reference line due to fringe line tilt.  The     **
;**   individual displacements are returned in the     **
;**   array DEL.                                       **
;*******************************************************
    DELTA3,IMAGE,DEL

;*******************************************************
;**   Performs the necessary spatial shift in the      **
;**   individual rows.  The FFT is taken of the row's  **
;**   interference pattern and then the shift is       **
;**   performed in the frequency domain.  The shifted  **
;**   data is then returned to the spacial domain      **
;**   using the reverse FFT.  The tilt corrected       **
;**   interference pattern is stored in the COMP       **
;**   matrix.                                          **
;*******************************************************
  F=SHIFT(FINDGEN(753)-376,377)/752.
  FOR M=0,243 DO BEGIN
       FCOMP=FFT(IMAGE(*,M),-1)
       FCOMP=FCOMP*COMPLEX(COS(2*!PI*DEL(M)*F),SIN(-2*!PI*DEL(M)*F))
       COMP(*,M)=FFT(FCOMP,1)
  ENDFOR
;  stop
;*******************************************************
;**   The matrix comp is collapsed in the vertical     **
;**   while coadding the rows to average out noise.    **
;**   The derivative of the resulting array is taken   **
;**   to remove the non-linear DC offset.  The first   **
;**   and last five data points are zeroed due to      **
;**   unusable data.                                   **
;*******************************************************
  DAT1=DERIV(TOTAL(COMP,2))
  DAT1(0:5)=0
  DAT1(748:752)=0

;*******************************************************
;**   By finding the maximum of the interferogram, the**
;**   a doubled-sided interferogram is created from    **
;**   the single-sided interferogram.  This double-    **
;**   sided array is stored in the array DAT.          **
;**   The number of points in the array DAT is note    **
;**   to be recorded later.                            **
;*******************************************************
```

69

```
  JUNK2=MAX(DAT1)
   A1=!C-1
      A2=!C
      A3=!C+1
      CENTER=(A3-$
      ((DAT1(A3)-DAT1(A2))/(DAT1(A3)-2*DAT1(A2)+DAT1(A1))+$
      .5))
  FDAT1=FFT(DAT1,-1)
  PCFDAT1=FDAT1*COMPLEX(COS(2*!PI*(CENTER-!C)*F),SIN(2*!PI*(CENTER-!C)*F))
  PCDAT1=FFT(PCFDAT1,1)
  IF !C LT 376   THEN BEGIN
      CORE=PCDAT1(!C:747)
  ENDIF ELSE BEGIN
      CORE=REVERSE(PCDAT1(6:!C)
  ENDELSE

  NPTS=N_ELEMENTS(CORE)
  DAT=COMPLEXARR(2*NPTS-1)
  DAT(0)=CORE
  DCORE=CORE(1:*)
  DAT(NPTS)=REVERSE(DCORE)
  DAT=FLOAT(DAT)

;********************************************************
;**   The spectrum of the interferogram is found by   **
;**   performing the FFT of the interferogram.  The   **
;**   spectrum stored in SPEC is plotted.  The array  **
;**   SPEC is returned when the program ends.          **
;********************************************************
  SPEC=FFT(WHANNING*(DAT-TOTAL(DAT)/(2*NPTS-1.)),-1)
 ; PLOT,SPEC
  SPEC(0)=NPTS
STOP
RETURN
END
```

70

```
PRO IMAGE,FILE,IMAGE

;******************************************************
;******************************************************
;**   This program was created to read a TIFF file **
;**   that contained an interference pattern from   **
;**   the All-Reflection Michelson Interferometer.  **
;**   The interference pattern was recorded using   **
;**   the software for the EDC 1000HR camera.       **
;******************************************************
;******************************************************


;******************************************************
;******************************************************
;**   Call Procedure Example                        **
;**                                                 **
;**   IMAGE,'20APR2',IMAGE                          **
;**                                                 **
;**   The above statement calls image (this         **
;**   program), inputs 20APR2 into FILE and calls   **
;**   that file to be read and stored into the      **
;**   array IMAGE and returns to system or main     **
;**   program.                                      **
;**                                                 **
;**   If file is not located in C:\CAMERA\D2        **
;**   then change directory in FILENAME as needed.  **
;******************************************************

FILENAME='D:\CAMERA\D2\'+FILE+'.TIF'
IMAGE=TIFF_READ(FILENAME)
RETURN
END
```

71

```
PRO  DELTA3,IMAGE,DEL

;***********************************************************
;***********************************************************
;**    This program was created to find the horizontal  **
;**    misalignment of each line of an interference      **
;**    pattern from the All-Reflection Michelson         **
;**    Interferometer.                                   **
;***********************************************************
;***********************************************************


;***********************************************************
;***********************************************************
;**    Call Procedure Example                            **
;**                                                      **
;**    DELTA3,IMAGE,DEL                                  **
;**                                                      **
;**    The above statement calls DELTA3 (this program)  **
;**    with the matrix IMAGE as an input.  The amount of**
;**    horizontal displacement from a reference line is **
;**    computed and store in the array DEL and returns   **
;**    to system or main program.                        **
;***********************************************************
;***********************************************************


;***********************************************************
;***********************************************************
;**    Designates line 122 as the reference line for    **
;**    comparison to find the horizontal displacements. **
;***********************************************************
;***********************************************************
  DEL=FLTARR(244)
  SCALE=8192/753.
  REF=IMAGE(*,122)-TOTAL(IMAGE(*,122))/753.
  FREF122=FFT(REF,-1)
  FREF=FREF122
  FCORR=COMPLEXARR(8192)
  MASK=(INDGEN(8192)LT 21) OR (INDGEN(8192)GT 8171)
  DEL(122)=0

;***********************************************************
;***********************************************************
;**    Starts at row 121 and works to the top of the    **
;**    IMAGE matrix to find each rows horizontal         **
;**    displacement from the reference rown #122.        **
;**                                                      **
;**    This is achieved by performing a correlation      **
;**    between the test row and the reference row.  The **
;**    maximum is then estimated by using a peak finding**
;**    algorithm. The horizontal deviation is stored    **
;**    in the array DEL                                  **
;***********************************************************
;***********************************************************
  FOR J=121,0,-1 DO BEGIN
    TEST=IMAGE(*,J)

;***********************************************************
;**    Test for row being zero                           **
;***********************************************************
    OFFSET=TOTAL(TEST)/753.
    IF OFFSET EQ 0 THEN BEGIN
       DELTA=0 & GOTO,SKIP1
    ENDIF
    TEST=TEST-OFFSET
```

73

```
;*******************************************************
;**   Correlation Procedure                         **
;*******************************************************
    FTEST=FFT(TEST,-1)
    FCOR=FREF*CONJ(FTEST)
    FCORR=FCORR*0
    FCORR(0)=FCOR(0:376)
    FCORR(8192-376)=FCOR(377:*)
    CORR=FLOAT(FFT(FCORR,1))

;*******************************************************
;**   Peak finding algorithm                        **
;*******************************************************
    GARBAGE=MAX(ABS(CORR*MASK))
      A1=!C-1 & IF A1 EQ -1 THEN A1=8191
      A2=!C
      A3=!C+1 & IF A3 EQ 8192 THEN A3=0
      DELTA=(A3-$
      ((CORR(A3)-CORR(A2))/(CORR(A3)-2*CORR(A2)+CORR(A1))+$
       .4992))/SCALE

;*******************************************************
;**   Storing the horizontal deviation DELTA in array **
;**   DEL                                            **
;*******************************************************
    IF DELTA GT 375 THEN DELTA=DELTA-753.
    IF ABS(DELTA) LT .0001 THEN DELTA=0
    FREF=FTEST
    SKIP1:  DEL(J)=DEL(J+1)+DELTA
  ENDFOR




;*******************************************************
;*******************************************************
;**   Starts at row 123 and works to the bottom of the **
;**   IMAGE matrix to find each rows horizontal      **
;**   displacement from the reference rown #122.     **
;**                                                  **
;**   This is achieved by performing a correlation   **
;**   between the test row and the reference row.  The **
;**   maximum is then estimated by using a peak finding**
;**   algorithm. The horizontal deviation is stored  **
;**   in the array DEL                               **
;*******************************************************
;*******************************************************
  FREF=FREF122
  FOR J=123,243 DO BEGIN
    TEST=IMAGE(*,J)

;*******************************************************
;**   Test for row being zero                        **
;*******************************************************
    OFFSET=TOTAL(TEST)/753.
    IF OFFSET EQ 0 THEN BEGIN
       DELTA=0 & GOTO,SKIP2
    ENDIF
    TEST=TEST-OFFSET

;*******************************************************
;**   Correlation Procedure                          **
;*******************************************************
    FTEST=FFT(TEST,-1)
    FCOR=FREF*CONJ(FTEST)
    FCORR=FCORR*0
    FCORR(0)=FCOR(0:376)
    FCORR(8192-376)=FCOR(377:*)
    CORR=FLOAT(FFT(FCORR,1))
```

74

```
;*********************************************************
;**   Peak finding algorithm                          **
;*********************************************************
    GARBAGE=MAX(ABS(CORR*MASK))
      A1=!C-1 & IF A1 EQ -1 THEN A1=8191
      A2=!C
      A3=!C+1 & IF A3 EQ 8192 THEN A3=0
      DELTA=(A3-$
      ((CORR(A3)-CORR(A2))/(CORR(A3)-2*CORR(A2)+CORR(A1))+$
       .4992))/SCALE

;*********************************************************
;**   Storing the horizontal deviation DELTA in array  **
;**   DEL                                              **
;*********************************************************
    IF DELTA GT 375 THEN DELTA=DELTA-753.
    IF ABS(DELTA) LT .0001 THEN DELTA=0
    FREF=FTEST
SKIP2:   DEL(J)=DEL(J-1)+DELTA
    ENDFOR


RETURN
END
```

75

LIST OF REFERENCES

Atkinson, J. D. IV, "Implementation and use of a computational ray-tracing program for the design and analysis of complex optical systems," Master's Thesis, Naval Postgraduate School, Monterey, California, (1993).

Barus, C., "The interferometry of reversed and nonreversed spectra," Carnegie Institution of Washington Publ. 149 (1911), part1.

Bush, B. C., D. M. Cotton, J. S. Vickers and S. Chakrabarti, "Instrument design and test results of the new all-reflection spatial heterodyne spectrometer," in EUV, X-Ray and Gamma-Ray Instrumentation for Astronomy II, Proc. Soc. Photo-Opt. Instrum. Eng., **1549**, 376-384, (1991).

Carlson, S. M., "Validation of the design of a high resolution all-reflection Michelson interferometer for atmospheric spectroscopy," ," Master's Thesis, Naval Postgraduate School, Monterey, California, (1993).

Cleary, D. D., S. Gnanalingam, R. P. McCoy, K. F. Dymond and F. G. Eparvier, "The middle ultraviolet dayglow spectrum," J. Geophys. Res., **100**, 9729-9739, (1995).

Davis, D. S., "A study of the spectrum and structure of the natural vanadium atom," Appendix A: Fundamental of Fourier Transform Spectroscopy, Ph.D. Dissertation, Perdue University, (1976).

Davis, D. S., H. P. Larson, M. Williams, G. Michel, P. Connes, "An infrared fourier spectrometer for airborne and ground-based astronomy," Appl. Opt., **19**, 4138-4155, (1980).

Gill, M. D., "Design, validation and prototype testing of a high resolution all-reflection Michelson interferometer for solar occultation measurements of the OI 1304-Å triplet emission," Master's Thesis, Naval Postgraduate School, Monterey, California, (1994).

Hamamatsu Photonics, Characteristics and Applications of Microchannel Plates, (1985).

Hymas, H. M., "A calibration of the Naval Postgraduate School middle ultraviolet spectrograph and a analysis of the OII 2470 Å emission obtained by the middle ultraviolet spectrograph," Master's Thesis, Naval Postgraduate School, Monterey, California, (1994).

Klein, M. V., T. E. Furtak, Optics, 2nd ed., John Wiley & Sons, New York, (**1986**).

Kruger, R. A., L. W. Anderson and F. L. Roesler, "All-reflection interferometer for use as a fourier-transform spectrometer," J. Opt. Soc. Am., **62**, 938-945, (1972).

Laprade, B. N., "The high output technology microchannel plate," in Image Intensification, Proc. Soc. Photo-Opt. Instrum. Eng., **1072**, 102-110, (1989).

MacQuarrie, J. A., "A ground support electronic interface for the ionospheric spectroscopy and atmospheric chemistry (ISAAC) ultraviolet spectrograph," Master's Thesis, Naval Postgraduate School, Monterey, California, (1994).

MacQuarrie, J. A., Private Conversation, (1994).

Milton Roy Company, Diffraction Grating Handbook, 2nd ed., (1994).

Nichols, J. W., "The design of a new far ultraviolet interferometer for ionospheric spectroscopy," Master's Thesis, Naval Postgraduate School, Monterey, California, (1990).

National Institute of Standards and Technology, Personal Communication, (1995)

Risley, A. D. Jr., "Development testing of a prototype all-reflection Michelson interferometer," Master's Thesis, Naval Postgraduate School, Monterey, California, (1993).

Samson, J. A. R., Techniques of Vacuum Ultraviolet Spectroscopy, John Wiley & Sons, New York, (1967).

Wallace, K. M. Jr., "Design of a high resolution spatial heterodyne interferometer," Master's Thesis, Naval Postgraduate School, Monterey, California, (1992).

Walters, D. L., PH4050 Class Notes, (1995).

Wolfe, W. L., G. J. Zissis, The Infrared Handbook, Office of Naval Research, Department of the Navy, Washington, DC (1978).

INITIAL DISTRIBUTION LIST

1. Defense Technical Information Center   2
    8725 John J. Kingman Rd., STE 0944
    Ft. Belvoir, Virginia 22060-6218

2. Library, Code 13   2
    Naval Postgraduate School
    Monterey, California 93943-5002

3. Dr. William B. Colson, Chairman PH   1
    Physics Department
    Naval Postgraduate School
    Monterey, California 93943-5002

4. Dr. D. D. Cleary, Code PH/CL   10
    Physics Department
    Naval Postgraduate School
    Monterey, California 93943-5002

5. Dr. Oscar Biblarz, Code AA/Bi   1
    Department of Aeronautics and Astronautics
    Naval Postgraduate School
    Monterey, California 93943-5160

6. LT Jeffrey D. Hicks   2
    5659 Bloomingdale Road
    Blountville, Tennessee 37617